Cross section for $b\bar{b}$ production via dielectrons in d + Au collisions at $\sqrt{s_{NN}} = 200$ GeV

A. Adare,[13] C. Aidala,[41,42] N. N. Ajitanand,[59] Y. Akiba,[55,56] H. Al-Bataineh,[49] J. Alexander,[59] A. Angerami,[14] K. Aoki,[33,55] N. Apadula,[60] Y. Aramaki,[12,55] E. T. Atomssa,[34] R. Averbeck,[60] T. C. Awes,[51] B. Azmoun,[7] V. Babintsev,[23] M. Bai,[6] G. Baksay,[19] L. Baksay,[19] K. N. Barish,[8] B. Bassalleck,[48] A. T. Basye,[1] S. Bathe,[5,8,56] V. Baublis,[54] C. Baumann,[43] A. Bazilevsky,[7] S. Belikov,[7,*] R. Belmont,[64] R. Bennett,[60] J. H. Bhom,[68] D. S. Blau,[32] J. S. Bok,[68] K. Boyle,[60] M. L. Brooks,[37] H. Buesching,[7] V. Bumazhnov,[23] G. Bunce,[7,56] S. Butsyk,[37] S. Campbell,[60] A. Caringi,[44] C.-H. Chen,[60] C. Y. Chi,[14] M. Chiu,[7] I. J. Choi,[68] J. B. Choi,[10] R. K. Choudhury,[4] P. Christiansen,[39] T. Chujo,[63] P. Chung,[59] O. Chvala,[8] V. Cianciolo,[51] Z. Citron,[60] B. A. Cole,[14] Z. Conesa del Valle,[34] M. Connors,[60] M. Csanád,[17] T. Csörgő,[67] T. Dahms,[60] S. Dairaku,[33,55] I. Danchev,[64] K. Das,[20] A. Datta,[41] G. David,[7] M. K. Dayananda,[21] A. Denisov,[23] A. Deshpande,[56,60] E. J. Desmond,[7] K. V. Dharmawardane,[49] O. Dietzsch,[58] A. Dion,[27,60] M. Donadelli,[58] O. Drapier,[34] A. Drees,[60] K. A. Drees,[6] J. M. Durham,[37,60] A. Durum,[23] D. Dutta,[4] L. D'Orazio,[40] S. Edwards,[20] Y. V. Efremenko,[51] F. Ellinghaus,[13] T. Engelmore,[14] A. Enokizono,[51] H. En'yo,[55,56] S. Esumi,[63] B. Fadem,[44] D. E. Fields,[48] M. Finger,[9] M. Finger, Jr.,[9] F. Fleuret,[34] S. L. Fokin,[32] Z. Fraenkel,[66,*] J. E. Frantz,[50,60] A. Franz,[7] A. D. Frawley,[20] K. Fujiwara,[55] Y. Fukao,[55] T. Fusayasu,[46] I. Garishvili,[61] A. Glenn,[36] H. Gong,[60] M. Gonin,[34] Y. Goto,[55,56] R. Granier de Cassagnac,[34] N. Grau,[2,14] S. V. Greene,[64] G. Grim,[37] M. Grosse Perdekamp,[24] T. Gunji,[12] H.-Å. Gustafsson,[39,*] J. S. Haggerty,[7] K. I. Hahn,[18] H. Hamagaki,[12] J. Hamblen,[61] R. Han,[53] J. Hanks,[14] E. Haslum,[39] R. Hayano,[12] X. He,[21] M. Heffner,[36] T. K. Hemmick,[60] T. Hester,[8] J. C. Hill,[27] M. Hohlmann,[19] W. Holzmann,[14] K. Homma,[22] B. Hong,[31] T. Horaguchi,[22] D. Hornback,[61] S. Huang,[64] T. Ichihara,[55,56] R. Ichimiya,[55] Y. Ikeda,[63] K. Imai,[28,33,55] M. Inaba,[63] D. Isenhower,[1] M. Ishihara,[55] M. Issah,[64] D. Ivanischev,[54] Y. Iwanaga,[22] B. V. Jacak,[60] J. Jia,[7,59] X. Jiang,[37] J. Jin,[14] B. M. Johnson,[7] T. Jones,[1] K. S. Joo,[45] D. Jouan,[52] D. S. Jumper,[1] F. Kajihara,[12] J. Kamin,[60] J. H. Kang,[68] J. Kapustinsky,[37] K. Karatsu,[33,55] M. Kasai,[55,57] D. Kawall,[41,56] M. Kawashima,[55,57] A. V. Kazantsev,[32] T. Kempel,[27] A. Khanzadeev,[54] K. M. Kijima,[22] J. Kikuchi,[65] A. Kim,[18] B. I. Kim,[31] D. J. Kim,[29] E.-J. Kim,[10] Y.-J. Kim,[24] E. Kinney,[13] Á. Kiss,[17] E. Kistenev,[7] D. Kleinjan,[8] L. Kochenda,[54] B. Komkov,[54] M. Konno,[63] J. Koster,[24] A. Král,[15] A. Kravitz,[14] G. J. Kunde,[37] K. Kurita,[55,57] M. Kurosawa,[55] Y. Kwon,[68] G. S. Kyle,[49] R. Lacey,[59] Y. S. Lai,[14] J. G. Lajoie,[27] A. Lebedev,[27] D. M. Lee,[37] J. Lee,[18] K. B. Lee,[31] K. S. Lee,[31] M. J. Leitch,[37] M. A. L. Leite,[58] X. Li,[11] P. Lichtenwalner,[44] P. Liebing,[56] L. A. Linden Levy,[13] T. Liška,[15] H. Liu,[37] M. X. Liu,[37] B. Love,[64] D. Lynch,[7] C. F. Maguire,[64] Y. I. Makdisi,[6] M. D. Malik,[48] V. I. Manko,[32] E. Mannel,[14] Y. Mao,[53,55] H. Masui,[63] F. Matathias,[14] M. McCumber,[60] P. L. McGaughey,[37] D. McGlinchey,[13,20] N. Means,[60] B. Meredith,[24] Y. Miake,[63] T. Mibe,[30] A. C. Mignerey,[40] K. Miki,[55,63] A. Milov,[7] J. T. Mitchell,[7] A. K. Mohanty,[4] H. J. Moon,[45] Y. Morino,[12] A. Morreale,[8] D. P. Morrison,[7,†] T. V. Moukhanova,[32] T. Murakami,[33] J. Murata,[55,57] S. Nagamiya,[30,55] J. L. Nagle,[13,‡] M. Naglis,[66] M. I. Nagy,[67] I. Nakagawa,[55,56] Y. Nakamiya,[22] K. R. Nakamura,[33,55] T. Nakamura,[55] K. Nakano,[55] S. Nam,[18] J. Newby,[36] M. Nguyen,[60] M. Nihashi,[22] R. Nouicer,[7] A. S. Nyanin,[32] C. Oakley,[21] E. O'Brien,[7] S. X. Oda,[12] C. A. Ogilvie,[27] M. Oka,[63] K. Okada,[56] Y. Onuki,[55] A. Oskarsson,[39] M. Ouchida,[22,55] K. Ozawa,[12] R. Pak,[7] V. Pantuev,[25,60] V. Papavassiliou,[49] I. H. Park,[18] S. K. Park,[31] W. J. Park,[31] S. F. Pate,[49] H. Pei,[27] J.-C. Peng,[24] H. Pereira,[16] D. Yu. Peressounko,[32] R. Petti,[7,60] C. Pinkenburg,[7] R. P. Pisani,[7] M. Proissl,[60] M. L. Purschke,[7] H. Qu,[21] J. Rak,[29] I. Ravinovich,[66] K. F. Read,[51,61] S. Rembeczki,[19] K. Reygers,[43] V. Riabov,[54] Y. Riabov,[54] E. Richardson,[40] D. Roach,[64] G. Roche,[38] S. D. Rolnick,[8] M. Rosati,[27] C. A. Rosen,[13] S. S. E. Rosendahl,[39] P. Ružička,[26] B. Sahlmueller,[43,60] N. Saito,[30] T. Sakaguchi,[7] K. Sakashita,[55,62] V. Samsonov,[47,54] S. Sano,[12,65] T. Sato,[63] S. Sawada,[30] K. Sedgwick,[8] J. Seele,[13] R. Seidl,[24,56] R. Seto,[8] D. Sharma,[66] I. Shein,[23] T.-A. Shibata,[55,62] K. Shigaki,[22] M. Shimomura,[63] K. Shoji,[33,55] P. Shukla,[4] A. Sickles,[7] C. L. Silva,[27] D. Silvermyr,[51] C. Silvestre,[16] K. S. Sim,[31] B. K. Singh,[3] C. P. Singh,[3] V. Singh,[3] M. Slunečka,[9] R. A. Soltz,[36] W. E. Sondheim,[37] S. P. Sorensen,[61] I. V. Sourikova,[7] P. W. Stankus,[51] E. Stenlund,[39] S. P. Stoll,[7] T. Sugitate,[22] A. Sukhanov,[7] J. Sziklai,[67] E. M. Takagui,[58] A. Taketani,[55,56] R. Tanabe,[63] Y. Tanaka,[46] S. Taneja,[60] K. Tanida,[33,55,56] M. J. Tannenbaum,[7] S. Tarafdar,[3] A. Taranenko,[47,59] H. Themann,[60] D. Thomas,[1] T. L. Thomas,[48] M. Togawa,[56] A. Toia,[60] L. Tomášek,[26] H. Torii,[22] R. S. Towell,[1] I. Tserruya,[66] Y. Tsuchimoto,[22] C. Vale,[7] H. Valle,[64] H. W. van Hecke,[37] E. Vazquez-Zambrano,[14] A. Veicht,[24] J. Velkovska,[64] R. Vértesi,[67] M. Virius,[15] V. Vrba,[26] E. Vznuzdaev,[54] X. R. Wang,[49] D. Watanabe,[22] K. Watanabe,[63] Y. Watanabe,[55,56] F. Wei,[27] R. Wei,[59] J. Wessels,[43] S. N. White,[7] D. Winter,[14] C. L. Woody,[7] R. M. Wright,[1] M. Wysocki,[13] Y. L. Yamaguchi,[12,55] K. Yamaura,[22] R. Yang,[24] A. Yanovich,[23] J. Ying,[21] S. Yokkaichi,[55,56] Z. You,[53] G. R. Young,[51] I. Younus,[35,48] I. E. Yushmanov,[32] W. A. Zajc,[14] and S. Zhou[11]

(PHENIX Collaboration)

[1]*Abilene Christian University, Abilene, Texas 79699, USA*

[2]*Department of Physics, Augustana College, Sioux Falls, South Dakota 57197, USA*

[3]*Department of Physics, Banaras Hindu University, Varanasi 221005, India*

[4]*Bhabha Atomic Research Centre, Bombay 400 085, India*

[5]*Baruch College, City University of New York, New York, New York, 10010, USA*

[6]*Collider-Accelerator Department, Brookhaven National Laboratory, Upton, New York 11973-5000, USA*

[7]*Physics Department, Brookhaven National Laboratory, Upton, New York 11973-5000, USA*

[8]*University of California - Riverside, Riverside, California 92521, USA*

[9]*Charles University, Ovocný trh 5, Praha 1, 116 36, Prague, Czech Republic*

[10]*Chonbuk National University, Jeonju, 561-756, Korea*
[11]*Science and Technology on Nuclear Data Laboratory, China Institute of Atomic Energy, Beijing 102413, P. R. China*
[12]*Center for Nuclear Study, Graduate School of Science, University of Tokyo, 7-3-1 Hongo, Bunkyo, Tokyo 113-0033, Japan*
[13]*University of Colorado, Boulder, Colorado 80309, USA*
[14]*Columbia University, New York, New York 10027 and Nevis Laboratories, Irvington, New York 10533, USA*
[15]*Czech Technical University, Zikova 4, 166 36 Prague 6, Czech Republic*
[16]*Dapnia, CEA Saclay, F-91191, Gif-sur-Yvette, France*
[17]*ELTE, Eötvös Loránd University, H - 1117 Budapest, Pázmány P. s. 1/A, Hungary*
[18]*Ewha Womans University, Seoul 120-750, Korea*
[19]*Florida Institute of Technology, Melbourne, Florida 32901, USA*
[20]*Florida State University, Tallahassee, Florida 32306, USA*
[21]*Georgia State University, Atlanta, Georgia 30303, USA*
[22]*Hiroshima University, Kagamiyama, Higashi-Hiroshima 739-8526, Japan*
[23]*IHEP Protvino, State Research Center of Russian Federation, Institute for High Energy Physics, Protvino, 142281, Russia*
[24]*University of Illinois at Urbana-Champaign, Urbana, Illinois 61801, USA*
[25]*Institute for Nuclear Research of the Russian Academy of Sciences, prospekt 60-letiya Oktyabrya 7a, Moscow 117312, Russia*
[26]*Institute of Physics, Academy of Sciences of the Czech Republic, Na Slovance 2, 182 21 Prague 8, Czech Republic*
[27]*Iowa State University, Ames, Iowa 50011, USA*
[28]*Advanced Science Research Center, Japan Atomic Energy Agency, 2-4 Shirakata Shirane, Tokai-mura, Naka-gun, Ibaraki-ken 319-1195, Japan*
[29]*Helsinki Institute of Physics and University of Jyväskylä, P.O.Box 35, FI-40014 Jyväskylä, Finland*
[30]*KEK, High Energy Accelerator Research Organization, Tsukuba, Ibaraki 305-0801, Japan*
[31]*Korea University, Seoul, 136-701, Korea*
[32]*Russian Research Center "Kurchatov Institute," Moscow, 123098 Russia*
[33]*Kyoto University, Kyoto 606-8502, Japan*
[34]*Laboratoire Leprince-Ringuet, Ecole Polytechnique, CNRS-IN2P3, Route de Saclay, F-91128, Palaiseau, France*
[35]*Physics Department, Lahore University of Management Sciences, Lahore 54792, Pakistan*
[36]*Lawrence Livermore National Laboratory, Livermore, California 94550, USA*
[37]*Los Alamos National Laboratory, Los Alamos, New Mexico 87545, USA*
[38]*LPC, Université Blaise Pascal, CNRS-IN2P3, Clermont-Fd, 63177 Aubiere Cedex, France*
[39]*Department of Physics, Lund University, Box 118, SE-221 00 Lund, Sweden*
[40]*University of Maryland, College Park, Maryland 20742, USA*
[41]*Department of Physics, University of Massachusetts, Amherst, Massachusetts 01003-9337, USA*
[42]*Department of Physics, University of Michigan, Ann Arbor, Michigan 48109-1040, USA*
[43]*Institut fur Kernphysik, University of Muenster, D-48149 Muenster, Germany*
[44]*Muhlenberg College, Allentown, Pennsylvania 18104-5586, USA*
[45]*Myongji University, Yongin, Kyonggido 449-728, Korea*
[46]*Nagasaki Institute of Applied Science, Nagasaki-shi, Nagasaki 851-0193, Japan*
[47]*National Research Nuclear University, MEPhI, Moscow Engineering Physics Institute, Moscow, 115409, Russia*
[48]*University of New Mexico, Albuquerque, New Mexico 87131, USA*
[49]*New Mexico State University, Las Cruces, New Mexico 88003, USA*
[50]*Department of Physics and Astronomy, Ohio University, Athens, Ohio 45701, USA*
[51]*Oak Ridge National Laboratory, Oak Ridge, Tennessee 37831, USA*
[52]*IPN-Orsay, Universite Paris Sud, CNRS-IN2P3, BP1, F-91406, Orsay, France*
[53]*Peking University, Beijing 100871, P. R. China*
[54]*PNPI, Petersburg Nuclear Physics Institute, Gatchina, Leningrad region, 188300, Russia*
[55]*RIKEN Nishina Center for Accelerator-Based Science, Wako, Saitama 351-0198, Japan*
[56]*RIKEN BNL Research Center, Brookhaven National Laboratory, Upton, New York 11973-5000, USA*
[57]*Physics Department, Rikkyo University, 3-34-1 Nishi-Ikebukuro, Toshima, Tokyo 171-8501, Japan*
[58]*Universidade de São Paulo, Instituto de Física, Caixa Postal 66318, São Paulo CEP05315-970, Brazil*
[59]*Chemistry Department, Stony Brook University, SUNY, Stony Brook, New York 11794-3400, USA*
[60]*Department of Physics and Astronomy, Stony Brook University, SUNY, Stony Brook, New York 11794-3800, USA*
[61]*University of Tennessee, Knoxville, Tennessee 37996, USA*
[62]*Department of Physics, Tokyo Institute of Technology, Oh-okayama, Meguro, Tokyo 152-8551, Japan*
[63]*Institute of Physics, University of Tsukuba, Tsukuba, Ibaraki 305, Japan*
[64]*Vanderbilt University, Nashville, Tennessee 37235, USA*
[65]*Waseda University, Advanced Research Institute for Science and Engineering, 17 Kikui-cho, Shinjuku-ku, Tokyo 162-0044, Japan*
[66]*Weizmann Institute, Rehovot 76100, Israel*

[67] *Institute for Particle and Nuclear Physics, Wigner Research Centre for Physics, Hungarian Academy of Sciences (Wigner RCP, RMKI) H-1525 Budapest 114, POBox 49, Budapest, Hungary*
[68] *Yonsei University, IPAP, Seoul 120-749, Korea*

(Received 22 May 2014; revised manuscript received 19 December 2014; published 26 January 2015)

We report a measurement of e^+e^- pairs from semileptonic heavy-flavor decays in $d+\mathrm{Au}$ collisions at $\sqrt{s_{NN}} = 200$ GeV. By exploring the mass and transverse-momentum dependence of the yield, the bottom decay contribution can be isolated from charm, and quantified by comparison to PYTHIA and MC@NLO simulations. The resulting $b\bar{b}$-production cross section is $\sigma_{b\bar{b}}^{d\mathrm{Au}} = 1.37 \pm 0.28\ (\mathrm{stat}) \pm 0.46\ (\mathrm{syst})$ mb, which is equivalent to a nucleon-nucleon cross section of $\sigma_{bb}^{NN} = 3.4 \pm 0.8\ (\mathrm{stat}) \pm 1.1\ (\mathrm{syst})\ \mu\mathrm{b}$.

DOI: 10.1103/PhysRevC.91.014907 PACS number(s): 25.75.Dw

I. INTRODUCTION

Collisions of heavy nuclei at the Relativistic Heavy Ion Collider (RHIC) at Brookhaven National Laboratory produce a quark-gluon plasma, which is a fundamentally new strongly coupled state of partonic matter [1–4]. There is extensive experimental evidence that partons lose energy while traversing the hot medium [5–7]. Many theoretical studies have been performed to determine the role of gluon radiation and collisional energy-loss processes [8,9], as well as to confront the data with predictions based upon anti-de Sitter/conformal field theory (AdS/CFT) [10].

The fate of a heavy quark traversing the plasma can help elucidate the mechanism of energy loss and how it differs for light and heavy quarks, because the quark mass affects gluon radiation in the medium [11]. Consequently, single electrons and positrons from the decays of mesons containing heavy quarks have been studied in various systems at both RHIC [12–14] and the Large Hadron Collider at CERN [15,16].

Differentiating among theoretical descriptions of the energy loss will be aided by comparing charm and bottom yields. To observe quark-gluon plasma effects on heavy quarks, it is crucial to compare $\mathrm{Au}+\mathrm{Au}$ data to a baseline measurement not dominated by the plasma. Typically, $p+p$ collisions are used to provide this baseline. There are also effects of cold nuclear matter on the production of heavy quarks, which can be studied by comparing $p+p$ to $p+\mathrm{Pb}$ or $d+\mathrm{Au}$. PHENIX has already reported modification in cold nuclear matter of spectra of single electrons from heavy-flavor decays at moderate p_T [13], of heavy flavor measured through e-μ correlations [17], and of J/ψ [18,19]. Of course, the bound state can be broken up in cold nuclear matter, so the $c\bar{c}$ and $b\bar{b}$ production cross sections in $d+\mathrm{Au}$ are of interest.

Clean c/b separation is difficult to achieve with single-lepton measurements, because the single-lepton spectrum contains both charm and bottom contributions. The B-decay contribution increases with p_T, and is comparable to the D-decay contribution at $p_T \gtrsim 3$ GeV/c [20,21]. PHENIX performed initial measurements of the charm and bottom cross sections in $p+p$ collisions via high-mass dielectrons [22] and electron-hadron correlations [20]. STAR also reported a $b\bar{b}$ cross section in $p+p$ collisions [14] measured through single-electron spectra.

Reconstructing heavy-flavor hadrons or measuring leptons with displaced vertices allows more direct separation of charm and bottom. However, such measurements require microvertex detectors or large data sets into a very large aperture with high-resolution hadron identification. PHENIX has a new silicon microvertex detector, but no $d+\mathrm{Au}$ data have been collected with it yet.

Dielectron spectra, which are double differential in mass and p_T, allow separation of regions dominated by charm from those dominated by bottom. The yield and shape of the mass and p_T spectra provide sensitivity to the heavy-flavor cross sections. Furthermore, the spectra can also encode information about the heavy-flavor-production mechanism via the dielectron correlations, which affect the shape of the dielectron mass and p_T spectra.

Initial-state effects such as gluon shadowing in the nucleus may affect heavy-quark cross sections because the dominant production channel at RHIC is gluon fusion. The shape of the mass and p_T distributions of charm- and bottom-decay electrons could additionally be sensitive to other effects, such as parton energy loss and rescattering in cold nuclear matter, for which evidence was recently reported [13]. While azimuthal correlations of the two leptons have advantages for studying the heavy-quark production process [17], analysis of dileptons as a function of mass and p_T is undertaken to separate charm and bottom contributions.

In this paper we report a high-statistics measurement of dielectrons in $d+\mathrm{Au}$ collisions to provide part of the necessary baseline information for quark-gluon-plasma studies. Section II describes the experimental apparatus and trigger. Section III presents details about the data analysis including electron identification, background subtraction, and efficiency corrections. The data are presented in Sec. IV, as double-differential spectra in mass and p_T. Expected sources of dielectrons and effects of the PHENIX acceptance are also discussed in this section. In Sec. V the results are compared to models of charm and bottom production to determine the heavy-flavor cross sections and examine the sensitivity to leading-order and next-to-leading-order quantum chromodynamics (QCD) descriptions of heavy-flavor physics. Section VI presents our summary and conclusions.

*Deceased
†PHENIX Co-Spokesperson: morrison@bnl.gov
‡PHENIX Co-Spokesperson: jamie.nagle@colorado.edu

II. EXPERIMENT

The data reported in this paper were collected during the 2008 RHIC $d+\mathrm{Au}$ run. The data were recorded with the PHENIX detector by using a minimum-bias (MB) trigger and an electron (ERT) trigger. A total of 1.7 and 3.1 billion events were analyzed, for the MB- and ERT-triggered samples, respectively. The ERT sample corresponds to 116.6 billion sampled MB events and an integrated luminosity of 58.6 nb^{-1} (equivalent to a nucleon-nucleon $\int Ldt = 23\ \mathrm{pb}^{-1}$).

A detailed description of the PHENIX detector is available in Ref. [23]. The detector comprises two central arm spectrometers that cover a pseudorapidity range $|\eta| < 0.35$ ($70^\circ < \theta < 100^\circ$), with 90° in ϕ, and the tops of each arm are separated by 67.5°. Tracks are reconstructed using hit information from the drift chambers (DCs) and from the first layer of the pad chambers (PCs) [24]. Each DC volume comprises 20 sectors, with each sector covering 4.5° in azimuth and $|\eta| < 0.35$. There are six wire modules in each sector, called X1, U1, V1, X2, U2, and V2. The X1 and X2 wires are parallel to the beam axis and record charged-particle trajectories in the plane perpendicular to the magnetic field. The U and V stereo wires are oriented at $\sim \pm 6^\circ$ angle relative to the X wires and contribute to the measurement of the z coordinate along the beam direction. The PCs provide additional space points along the trajectory of charged particles, which are used to determine the polar angle θ and z coordinate of the track. The magnitude of the particle's bend in the central axial magnetic field is determined from the reconstructed track and used to determine the track's momentum. The momentum resolution for this data set is $\delta p/p = 0.011 \oplus 0.0116p$ [GeV/c].

Two ring-imaging Čerenkov (RICH) detectors with CO_2 as radiator gas are used for electron identification. They provide an e/π rejection of $\sim 10^{-3}$ for tracks with momenta below the pion Čerenkov threshold of ~ 4 GeV/c. Each detector contains spherical mirror panels, which focus Čerenkov light onto an array of 2560 photomultiplier tubes (PMTs). An average of 10 photons per $\beta \approx 1$ particle are emitted under the angle $\theta_c(1/(n\beta)) \approx 9$ mrad and get focused to a ring on the PMT array with a diameter of about 11.8 cm. Further electron identification is provided by the electromagnetic calorimeters (EMCals) that measure the position and energy of photons and electrons. Each arm comprises four rectangular sectors in ϕ. The two bottom sectors in one arm are constructed of 9216 lead-glass Čerenkov towers (PbGl) each, with a granularity of 4×4 cm^2 and a depth of $14.4X_0$. The rest of EMCal sectors are made of 15 552 lead-scintillator towers (PbSc) with a granularity of 5.5×5.5 cm^2 and a depth of $18X_0$. The spatial resolution of the PbSc(PbGl) EMCal sectors is $\sigma(E) = 1.55\,(0.2) \oplus 5.7\,(8.4)/\sqrt{E\ [\mathrm{GeV}]}$ mm for particles at normal incidence. The energy resolution of the PbSc(PbGl) calorimeters is $\delta E/E = 2.2\,(0.8\%) \oplus 8.1\,(5.9)/\sqrt{E\ [\mathrm{GeV}]}\%$.

The collision vertex, collision time, and minimum-bias trigger are provided by a pair of beam-beam counters (BBCs) located 144 cm from the center of PHENIX, on either side of the collision region. Each BBC comprises 64 quartz Čerenkov counters and covers full azimuth and a rapidity range of $3.1 < |\eta| < 3.9$. The collision vertex resolution is approximately 0.5 cm in $d+\mathrm{Au}$ collisions. The minimum bias trigger requires a coincidence between both BBCs, with at least one hit on each side, and that the vertex is within 38 cm of the nominal interaction point. The minimum bias trigger accepts $88 \pm 4\%$ of all inelastic $d+\mathrm{Au}$ collisions [25].

Fewer than 1% of minimum bias triggered events contain a single electron ($p_T > 200$ MeV) in the central arm acceptance. Consequently, only a tiny fraction of the events contains e^+e^- pairs and, of those, most are from pseudoscalar and vector meson decays. To accumulate a significant sample of e^+e^- pairs from heavy-flavor production, an electron trigger is critical. The electron trigger selects electron or positron candidates through Čerenkov light in the RICH which matches a shower in the EMCal on a potential particle trajectory. The ERT trigger is segmented into EMCal supermodules and RICH trigger tile. An EMCal supermodule is a group of 12×12 (or 6×4) PbSc (or PbGl) towers [26], while the RICH tiles group 4×5 PMTs. Matching between tiles and supermodules is implemented through lookup tables that depend on the shower energy. Two different energy thresholds on the shower, 600 and 800 MeV, were used for different periods of data taking.

III. DATA ANALYSIS

Data quality cuts include fiducial cuts to remove any detector-edge effects or dead areas. The data were collected into run groups with similar detector performance characteristics. Each group was analyzed separately, and the groups were combined after efficiency correction.

A. Electron identification

Electrons in the range $0.2 < p_T < 20$ GeV/c are identified by hits in the RICH and by matching the momentum with the energy measured in the EMCal. Table I summarizes the cuts relevant to this analysis. A description of each variable is given below.

(i) DC track quality: This bit pattern characterizes the quality of the track reconstruction. Tracks that have multiple hits in the X1 and X2 sections and have a unique PC1 hit, which is confirmed by the U, V sections are recorded as quality 63. If the U, V information is missing the quality is 51, and if there are multiple possible PC1 hits, but unique U, V information the quality is 31.

TABLE I. Electron ID cuts used in the analysis.

eID variable	Cut value
DC track quality	63||31||51
RICH n0	$\geqslant 2$
RICH χ^2/npe0	<10
EMCal energy	>150 MeV
E/p	>0.5
EMCal matching	$\sqrt{\sigma^2_{\Delta\phi} + \sigma^2_{\Delta z}} < 5.0$
γ conversions in support structures	See text

(ii) RICH n0: Number of hit RICH PMTs in a region with an inner radius of 3.4 cm and outer radius of 8.4 cm around the track projection on the RICH. The expected radius of a Čerenkov ring emitted by an electron is 5.9 cm.
(iii) RICH χ^2/npe0: A χ^2-like shape variable of the RICH ring associated with the track divided by the number of photoelectrons measured in a given ring (npe0).
(iv) EMCal energy: Energy deposited in EMCal cluster.
(v) *E/p*: A variable quantifying energy-momentum matching, where E is the energy measured by EMCal and p is the momentum of the track. For electrons, this quantity is approximately a Gaussian distribution around 1.0.
(vi) EMCal match ($\sigma_{\Delta\phi}$): Displacement in ϕ between the position of the associated EMCal cluster and the projection of the track onto the EMCal. This is measured in units of momentum-dependent resolution and is optimized for electrons.
(vii) EMCal match ($\sigma_{\Delta z}$): Analogous to the previous variable, for the z coordinate.
(viii) γ conversions in detector support structures: These are identified in a two-dimensional plane of DC-hit azimuthal angle versus E/p. Conversion electrons have shorter path length through the magnetic field, and consequently their momentum (and therefore their E/p) is misreconstructed.

The resulting electron purity is approximately 85%–90% [27].

B. Pair cuts

To fully control the kinematic edge of the single electron p_T cut, the pair $m_T = (m^2 + p_T^2)^{1/2}$ is required to be greater than 450 MeV/c. Additionally, for the ERT-triggered data, it is required that at least one of the tracks in any given pair fires the ERT trigger and that the p_T of that track is larger than 0.7 and 1 GeV/c, for the two different trigger thresholds, respectively. The values are chosen to ensure that the trigger efficiency is always larger than 25%.

There are two more pair cuts used in the analysis, as described below. Fully reconstructed conversions in the beam pipe and air before the DC are removed by a cut on a pairwise variable ϕ_V defined as

$$\vec{u} = \frac{\vec{p}_1 + \vec{p}_2}{|\vec{p}_1 + \vec{p}_2|}, \tag{1}$$

$$\vec{v} = \vec{p}_1 \times \vec{p}_2, \tag{2}$$

$$\vec{w} = \vec{u} \times \vec{v}, \tag{3}$$

$$\vec{u}_a = \frac{\vec{u} \times \hat{z}}{|\vec{u} \times \hat{z}|}, \tag{4}$$

$$\phi_V = \arccos\left(\frac{\vec{w} \cdot \vec{u}_a}{|\vec{w}||\vec{u}_a|}\right). \tag{5}$$

Here, $\vec{p}_1$ is the three-momentum vector of the electron and $\vec{p}_2$ is the three-momentum vector of the positron. This is a cut on the orientation of the plane defined by the opening angle of the pair with respect to the magnetic field, which is parallel to the beam axis $\vec{z}$. The e^+e^- pairs from photon conversions have no intrinsic opening angle. Therefore, the only way the two electrons from a conversion can be separated from each other is by the magnetic field pulling them apart. In this case, the opening angle will be aligned perpendicular to the magnetic field. However, any pair that decays from a source with mass must have an opening angle that is randomly oriented with respect to the magnetic field. For $m_{ee} < 600$ MeV/c^2, this cut removes 98% of the conversions while retaining 80% of the signal pairs. At higher pair mass, where the contribution from conversions are negligible, the cut removes 1.5% of the pair yield independent of mass.

An additional source of contamination in the dielectron spectrum is due to hadron tracks that share a RICH ring with an electron. The sharing cannot be properly reproduced by event mixing, so this contamination must be removed before background subtraction. As like-sign electron-hadron pairs populate a different region in mass and p_T from unlike-sign pairs, like-sign subtraction also cannot be used to remove this contamination. Consequently, a cut is placed on the distance between the projection of any two tracks onto the RICH photomultiplier-tube plane. If the projections are within 10σ in $\Delta\phi_{\rm RICH} \oplus \Delta z_{\rm RICH}$ (this corresponds to ≈36 cm, roughly twice the predicted maximum diameter of a RICH ring), then the entire event is rejected. This cut does not affect the mass spectrum above $m_{ee} > 600$ MeV/c^2 and removes less than 1% of the events [28].

C. Background subtraction

All electrons and positrons in a given event are combined into pairs. We refer to these as *foreground* and denote the number of e^+e^- pairs as N_{+-} and the like-sign pairs as $N_{\pm\pm}$. The foreground pairs contain signal pairs (S_{+-}) from the sources that we are interested in, and background pairs. Electrons and positrons from different physical sources ($B_{+-}^{\rm comb}$) are uncorrelated. Additionally, there are some e^+e^- background pairs which are correlated ($B_{+-}^{\rm cor}$), described in Sec. III C 1. Both types of background are subtracted statistically from the foreground to extract the signal.

Since the background is typically larger than the signal, the background estimation requires precision of a few percent. The signal-to-background (S/B) ratio varies with invariant mass of the pairs. In d + Au collisions, the p_T integrated S/B is larger than 1.0 only near the vector meson masses. It is below 0.1 for the low-mass continuum (<1.0 GeV/c^2). In the intermediate-mass continuum (1.0–3.0 GeV/c^2), the S/B is roughly constant between 0.2–0.3; the S/B increases for higher mass.

There are two different approaches to estimate the background: (i) the like-sign subtraction technique based on the measured like-sign foreground $N_{\pm\pm}$ or (ii) the event-mixing technique. In the PHENIX experiment, the acceptance for like- and unlike-sign pairs is different due to the two arm geometry and thus the shape of the invariant mass distributions are different, as illustrated in Fig. 1. We therefore traditionally have used the event-mixing technique. In this method, combinatorial background is estimated by taking an electron from

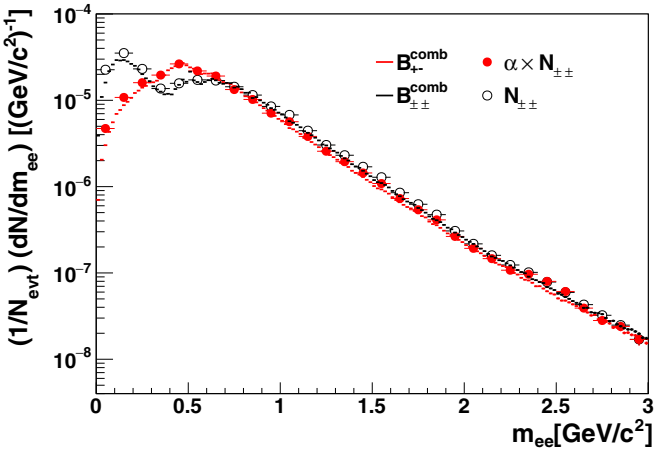

FIG. 1. (Color online) Mass distribution for the combinatorial background determined by event mixing B^{comb}_{+-} and $B^{comb}_{\pm\pm}$as the red and black line, respectively. The shape difference due to the difference in acceptance between like-sign and unlike-sign pairs in PHENIX is clearly visible. Also shown are foreground like-sign pairs $N_{\pm\pm}$(black points) and $N_{\pm\pm}$corrected for the acceptance difference (red points). The differences between points and lines are the correlated background.

event i and pairing it with a positron from event j ($\neq i$). This is a powerful approach because it allows for an extremely high statistics estimation of the background [28]. However, such an estimation must be normalized with a precision much better than the S/B. In addition, the mixed-event spectra do not contain any of the correlated background and therefore these additional pairs must be estimated by using Monte Carlo methods.

In this paper we use the like-sign subtraction technique, which avoids the complications inherent in the mixed-event-background estimation. The correction for the acceptance difference between like- and unlike-sign pairs is described in Sec. III C 2.

1. Correlated background

There are two sources of correlated background: *cross pairs* and *jet pairs* [22]. Cross pairs are correlated through a hadron decay that results in two e^+e^- pairs. These pairs originate from π^0 and η^0 double-Dalitz decays [$\pi^0(\eta) \to \gamma^*\gamma^* \to e^+e^-e^+e^-$], a single-Dalitz decay accompanied by a photon conversion [$\pi^0(\eta) \to \gamma\gamma^* \to e^+e^-e^+e^-$], and diphoton decays with both photons converting [$\pi^0(\eta) \to \gamma\gamma \to e^+e^-e^+e^-$]. The cross-pair correlation arises because of the small opening angle between the virtual and/or real decay photons. The resulting dielectrons tend to manifest at low mass and high p_T.

Jet pairs are the other major source of correlated e^+e^- background. In this case, the electron and positron are decay products of different hadrons inside jets. Dijet production and fragmentation causes a correlation in the parent hadrons, which is inherited by the daughter electrons. When the electron and positron are from opposing (back-to-back) jets, the pair typically has low p_T and high mass. When they arise from two hadrons in the same jet, the pair typically has high p_T and low mass.

Since cross pairs and jet pairs result from two e^+e^- pairs, correlated pairs with like and unlike sign are produced at the same rate. This fact can be exploited to correct for correlated background in the unlike-sign distribution.

2. Like-sign subtraction

The like-sign subtraction technique uses the foreground like-sign pairs $N_{\pm\pm}$ to determine the background. This has two distinct advantages over the event-mixing technique. First, the measured yield $N_{\pm\pm}$ requires no additional absolute normalization. The second advantage, which was mentioned in the previous section, is that $N_{\pm\pm}$ contains the identical amount of correlated background as the measured e^+e^- pairs N_{+-}. Hence, no independent simulation of the correlated background is needed.

This method, however, can be used in PHENIX only after correcting for the different acceptance for like-sign and unlike-sign pairs of the two-arm configuration (see Fig. 1). This correction is provided by the ratio of the acceptance functions for unlike- and like-sign pairs, the relative acceptance correction, α, which is due solely to the detector geometry and is determined by using mixed events as follows:

$$\alpha\,(m, p_T) = \frac{B^{comb}_{+-}\,(m, p_T)}{B^{comb}_{\pm\pm}\,(m, p_T)}. \tag{6}$$

The ratio of mixed-event unlike-sign to like-sign pairs is calculated differentially in mass and p_T and is applied to each run group separately.

Figure 1 shows the mass distribution for the unlike- and like-sign pairs in mixed events, $B^{comb}_{+-}$and $B^{comb}_{\pm\pm}$, respectively. Also shown is the mass spectrum for like-sign pairs $N_{\pm\pm}$. The relative acceptance correction translates $N_{\pm\pm}$ to the unlike-sign pair space via $N_{+-} = \alpha N_{\pm\pm}$. Deviations between the α-corrected like-sign spectrum and the unlike-sign mixed events correspond to the cross pairs and jet pairs.

The subtraction procedure is illustrated in Fig. 2. It illustrates the steps to transform the measured e^+e^- pairs N_{+-}in Fig. 2(a) to the signal of interest, S_{+-}, in Fig. 2(c). Figure 2(a) shows N_{+-}, B^{comb}_{+-}, and their difference, which corresponds to the signal S_{+-} plus the correlated background B^{cor}_{+-}. Figure 2(b) shows B^{cor}_{+-} calculated as the difference, $\alpha N_{\pm\pm} - B^{comb}_{+-}$. The signal S_{+-} is given in Fig. 2(c). The actual background subtraction is done double differentially and separately for each run group, as well as separately for minimum-bias and electron-triggered events:

$$\begin{aligned} S_{+-}(m, p_T) &= N_{+-}(m, p_T) - B^{comb}_{+-} - B^{cor}_{+-} \\ &= N_{+-}(m, p_T) - \alpha(m, p_T) N_{\pm\pm}(m, p_T). \end{aligned} \tag{7}$$

For the electron-triggered events, the trigger used in the data collection biases the single-electron distribution towards high p_T and as such the triggered events cannot be mixed with each other. Thus to generate the correct combinatorial background shape of e^+e^- pairs, the mixed events are generated from the minimum-bias data sample, but as in the real events, they are required to satisfy the trigger requirement. Every mixed pair

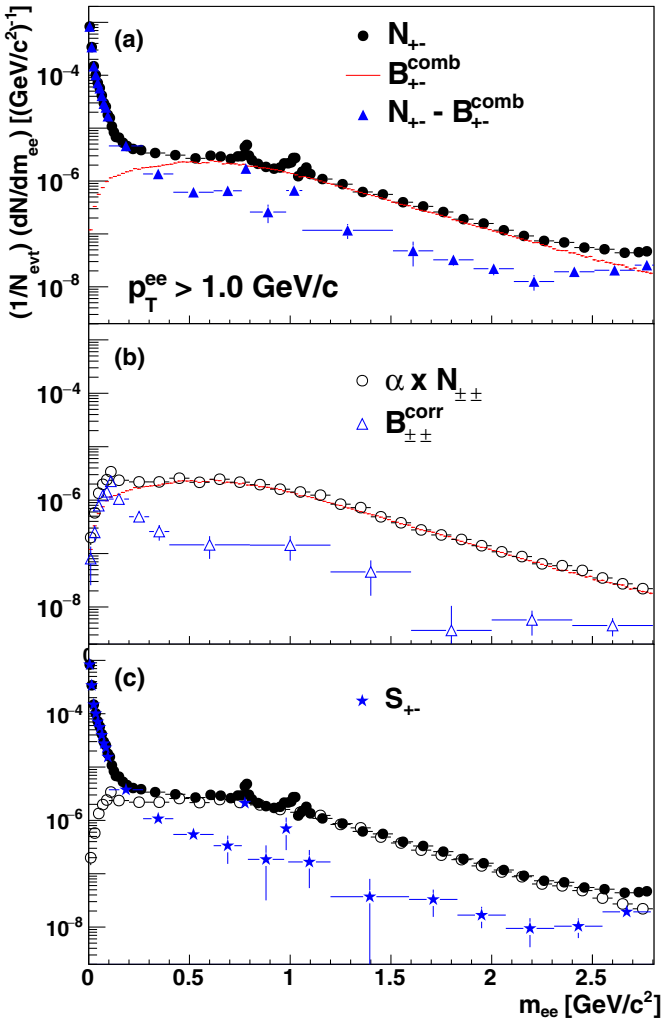

FIG. 2. (Color online) The top panel shows the e^+e^- pair foreground N_{+-}, the combinatorial background $B_{+-}^{\rm comb}$ determined through event mixing, and the difference of the two which is the sum of the signal we are interested in, S_{+-}, and the correlated background $B_{+-}^{\rm cor}$ that still needs to be subtracted. Shown in the middle panel is the estimate of the correlated background $B_{+-}^{\rm cor}$, which is the difference between the foreground like-sign pairs $N_{\pm\pm}$ corrected for the relative acceptance difference α between $N_{\pm\pm}$and N_{+-}[see Fig. 1 and Eq. (6)] and the combinatorial background $B_{+-}^{\rm comb}$. The bottom panel shows the signal S_{+-} which is calculated as $N_{+-} - \alpha N_{\pm\pm}$. In this plot, the combinatorial background is normalized in a region with minimal correlated background [22].

therefore contains at least one electron that fulfills the trigger condition [29].

3. B meson decay chains

The main decay chains for B and D mesons to ee pairs are shown in Table II. While for $c\bar{c}$, only the direct semileptonic decays, (1c) in Table II, contribute, many more possibilities exist for $b\bar{b}$. Decay combinations (1b)(1b) and (2b)(2b) lead to e^+e^- pairs, while combinations (2b)(1b) and (1b)(2b) lead to e^-e^- and e^+e^+ pairs due to the flavor change in the decay. The last decay chain (3b) involves the decay of a single b or $\bar{b}$ and produces only e^+e^- pairs. Since the semileptonic decay channels for B and D mesons have approximately equal branching ratios, and more than 90% of B mesons decay to D, all three groups of decays are approximately equally likely. This results in about a third of all ee pairs from $b\bar{b}$ decays being like-sign pairs, which get removed from the signal S_{+-}if one uses a like-sign subtraction technique.

TABLE II. Summary of the most relevant $c\bar{c}$ and $b\bar{b}$ decay chains that contribute to e^+e^- pairs. The effective branching ratio averages over all possible meson combinations.

Mode	Decay chain	Effective B.R.
(1c)	$D \to e^+X$	9.4%
(1b)	$B \to e^+X$	11%
(2b)	$B \to \bar{D}X \to e^-X'$	8.5%
(3b)	$B \to \bar{D}e^+X \to e^+e^-X'$	0.8%

Another important difference between ee pair production from $b\bar{b}$ compared to $c\bar{c}$ is that particle-antiparticle oscillations between B^0 and $\bar{B}^0$ can change one of the charges in an ee pair [30]. A B_d^0 oscillates with a probability of ~17% while a B_s^0 does so ≈49% of the time [31]. Therefore, in the all decay-chain combinations involving (1b) or (2b) from Table II, there is 20% probability for a sign change.

It is thus vital to treat the simulations with the same procedure as the data to properly account for all of the heavy-flavor pairs. Both PYTHIA [32] and Monte Carlo at next-to-leading-order (MC@NLO) [33] calculations generate the proper like-sign yield from heavy-flavor sources. As in the data analysis, we subtract this like-sign contribution from the unlike-sign yield in the simulations. Only then are comparisons made with the data.

D. Efficiency corrections

The e^+e^- signal S_{+-} for a given pair with mass m and transverse momentum p_T is corrected for the pair reconstruction efficiency $\varepsilon_{\rm rec}(m,p_T)$ and pair trigger efficiency $\varepsilon_{\rm ERT}(m,p_T)$ to obtain the e^+e^- yield in the PHENIX aperture:

$$\frac{d^2N}{dm_{e^+e^-}dp_T^{e^+e^-}} = \frac{1}{N_{\rm evt}^{\rm sampled}} \cdot \frac{1}{\Delta m_{e^+e^-}} \cdot \frac{1}{\Delta p_T^{e^+e^-}} \cdot \frac{1}{\varepsilon_{\rm rec}(m,p_T)} \cdot \frac{1}{\varepsilon_{\rm ERT}(m,p_T)} \cdot S_{+-}(m,p_T) \cdot C_{\rm bias}. \quad (8)$$

The factor $C_{\rm bias} = 0.889 \pm 0.003$ accounts for the autocorrelation between, having particles in the central arm spectrometers and the charge deposited in the BBC [25], as well as any inefficiency in the BBC trigger. It is calculated in a Glauber Monte Carlo-based framework that includes the BBC response. The corrected yield represents the heavy-flavor yield corresponding to the inelastic $d+$Au cross section of $\sigma_{\rm inel}^{d\rm Au} = 2.3 \pm 0.1$ b [25].

To evaluate the reconstruction efficiency $\varepsilon_{\rm rec}(m,p_T)$, 40M e^+e^- pairs are generated with constant yield in m, p_T, ϕ, $|y| < 1$. Of these, 20M are in the range $0 < m_{e^+e^-} < 16$ GeV/c^2 and $0 < p_T < 9$ GeV/c and, to increase statistics, another 20M

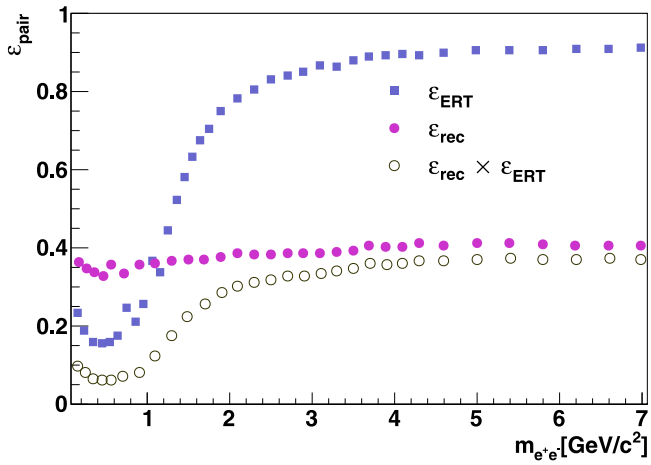

FIG. 3. (Color online) p_T-integrated pair reconstruction efficiency (solid magenta circles), pair trigger efficiency (solid blue squares), and the product of the two (open black circles).

are generated in a more limited range in $[m, p_T]$ covering $0 < m_{e^+e^-} < 2$ GeV/c^2 and $0 < p_T < 2$ GeV/c. The electron and positron are then filtered through the PHENIX acceptance.[1]

The remaining pairs are processed through a full GEANT3 simulation of the PHENIX detector [34] that includes the details of the detector response. The output files are then processed by the event reconstruction chain of PHENIX by applying the same cuts as for the data, which are listed in Table I. Each pair is weighted with the expected yield from hadron decays for that $[m, p_T]$. The ratio of reconstructed pairs to generated pairs then gives the efficiency $\varepsilon_{\rm rec}(m, p_T)$, which accounts for losses due to dead areas in the detector, track reconstruction efficiency, electron identification cuts, and e^+e^--pair cuts. The efficiency is evaluated separately for each run group. Figure 3 shows the p_T-integrated reconstruction efficiency as a function of pair mass for one run group. The efficiency is approximately 40% and varies only slightly with mass.

The inverse $[\varepsilon_{\rm rec}(m, p_T)]^{-1}$ is used to correct the S_{+-} to represent the yield in the PHENIX acceptance. It is applied double differentially in mass and p_T. More details about the mass and p_T dependence of the reconstruction efficiency can be found in Ref. [29]. We do not correct the data to represent pairs in a given rapidity range nor 2π in azimuth. This correction depends on the opening angle between the electron and positron and hence on the pair production process.

In addition to the reconstruction efficiency, the data need to be corrected for the efficiency of the ERT trigger $\varepsilon_{\rm ERT}(m, p_T)$. Since the ERT trigger fires on a single electron in a given event, the trigger efficiency for single electrons can be measured from data as

$$\varepsilon^e_{\rm ERT} = \frac{dN^{\pm}_{\rm MB\&\&ERT}/dp^{\pm}_T}{dN^{\pm}_{\rm MB}/dp^{\pm}_T}, \tag{9}$$

where $dN^{\pm}_{\rm MB\&\&ERT}/dp^{\pm}_T$ represents the p_T distribution of electrons that fire the ERT trigger in MB events and $dN^{\pm}_{\rm MB}/dp^{\pm}_T$ corresponds to the inclusive p_T distribution in MB events. The trigger efficiency is evaluated separately for each EMCal supermodule and RICH trigger tile. The energy threshold varies slightly from supermodule to supermodule. About 90% of the supermodules and tiles are fully operational and have 100% efficiency well above the trigger threshold. How quickly full efficiency is reached depends on energy resolution, as well as on the energy lost at the edges of supermodules. The remaining supermodules and tiles do not contribute to the trigger.

The effect of the ERT trigger efficiency on the e^+e^- pairs is calculated with a Monte Carlo simulation. For every simulated e^+e^- pair at least one of the tracks needs to be accepted in the corresponding EMCal supermodule and RICH tile. The pair trigger efficiency is calculated by dividing the number of e^+e^- pairs that were accepted by the total e^+e^- pairs without emulating the trigger. The blue points in Fig. 3 show the mass dependence of pair ERT efficiency determined from the simulations for the 600 MeV trigger threshold. We compared the pair mass and p_T distributions from MB events to the distributions from the triggered events corrected for the trigger efficiency. The distributions are identical within 5% in mass out to the J/ψ mass and in pair p_T out to 4 GeV/c, limited by the statistics of the MB data sample.

E. Systematic uncertainties

The systematic uncertainties on the e^+e^- yield arise from uncertainties on the dielectron reconstruction efficiency, the single-electron trigger efficiency, and the precision of the background determination.

The uncertainty in electron reconstruction is based on the reproducibility of the final result using multiple-cut variations both on single electrons and on electron pairs. The cuts varied include electron identification, conversion rejection, and pair cuts [27,29]. The conversion rejection and pair cuts are less influential and only affect the low-mass region ($<$600 MeV/c^2). The uncertainties are evaluated by reconstructing simulated dielectrons by using a full GEANT3 Monte Carlo simulation of the PHENIX detector. Detector dead areas can vary slightly within a given performance-based run group. Typical run-by-run variations were analyzed in addition to group-by-group variations to evaluate the systematic uncertainties from detector performance. In the intermediate (1–3 GeV/c^2) and high-mass regions ($>$3 GeV/c^2), these uncertainties vary between 10%–20%.

The precision of the trigger-efficiency correction depends on the available statistics in the minimum-bias data sample as well as on the supermodule segmentation of the EMCal. The triggered data are used above pair $m_T > 1.5$ GeV/c and contribute only a 5% uncertainty to the final result.

The dominant source of systematic uncertainty is the accuracy of the relative-acceptance correction. Since it is a

[1]The PHENIX acceptance is parametrized as function of the azimuthal angle ϕ of a track, its p_T, and charge sign q by conditions for the DC and the RICH for each spectrometer arm separately: $\phi_{\rm min} < \phi + qk_{\rm DC}/p_T < \phi_{\rm max}$ and $\phi_{\rm min} < \phi + qk_{\rm RICH}/p_T < \phi_{\rm max}$. The parameters are $k_{\rm DC} = 0.206$ rad GeV/c, $k_{\rm RICH} = 0.309$ rad GeV/c, $\phi_{\rm min} = -3/16\pi$ to $\phi_{\rm max} = 5/16\pi$, and $\phi_{\rm min} = 11/16\pi$ to $\phi_{\rm max} = 19/16\pi$.

TABLE III. Systematic uncertainties of the dilepton yield due to different sources with an indication of the applicable mass range. The transverse mass is defined as $m_T = (m^2 + p_T^2)^{1/2}$.

Component	Syst. uncertainty	Mass (GeV/c^2)
Pair reconstruction	14%	0–14
Conversion rejection	6%	0–0.6
	0%	>0.6
Pair cuts	5%	0.4–0.6
Trigger efficiency	5%	$m_T \geqslant 1.5$
Dead area, run groups	15%	0–2.5
	10%	2.5–14
Relative acceptance	5%·B/S	0–2.5
	2%·B/S	2.5–5
	1%·B/S	>5

mass- and p_T-dependent scale factor applied directly to the background, it affects the overall uncertainty in proportion to the background-to-signal ratio. This correction is very sensitive to the fluctuations in detector dead area that exist within a run group. Dedicated Monte Carlo simulations were performed to determine the effect of removing or including various regions of the PHENIX central arms. These regions were chosen to reflect realistic geometry including EMCal modules and supermodules, DC wires grouped by power input and signal output, and shifted positions of intrusive support structures. This uncertainty ranges from <5% at high mass (>5 GeV/c^2) to ∼25% below 2.5 GeV/c^2.

Table III summarizes the magnitude of the systematic uncertainty arising from various sources and the affected mass ranges.

IV. RESULTS

A. Yield of e^+e^- pairs

Figure 4 shows the mass projection of the measured double-differential e^+e^--pair yield in the PHENIX acceptance (as described in footnote 1). The inset shows the mass spectrum up to 4.5 GeV/c^2, and a detailed cocktail of hadronic decay sources that contribute to the mass spectrum below 4.5 GeV/c^2. The main figure shows the mass distributions of charm, bottom, and Drell–Yan e^+e^- pairs obtained by using PYTHIA. One can clearly see that the resonances lie atop a continuum, which is dominated by three-body decays of pseudoscalar and vector mesons for masses below 1.0 GeV/c^2. Above 1.0 GeV/c^2 the continuum is dominated by pairs from semileptonic decays of heavy flavor, with the bottom contribution becoming more important at higher mass.

The lower panel of the Fig. 4 shows the ratio of data to the expected sources. The shape of the measured mass spectrum is well described by the expected sources over the entire mass range. For the mass range below 1.0 GeV/c^2, the cocktail is absolutely normalized and shows a good agreement with the data. For the high-mass region, the e^+e^--pair continuum from heavy-flavor decays is normalized to the data to extract the bottom and charm cross section as discussed below.

B. Expected sources of e^+e^- pairs

Many sources contribute to the inclusive e^+e^- pair yield, so an in-depth understanding of the expected sources and their double differential distribution in e^+e^- pair mass and p_T is necessary to interpret the data. We use the detailed component-by-component simulation developed in Ref. [28]

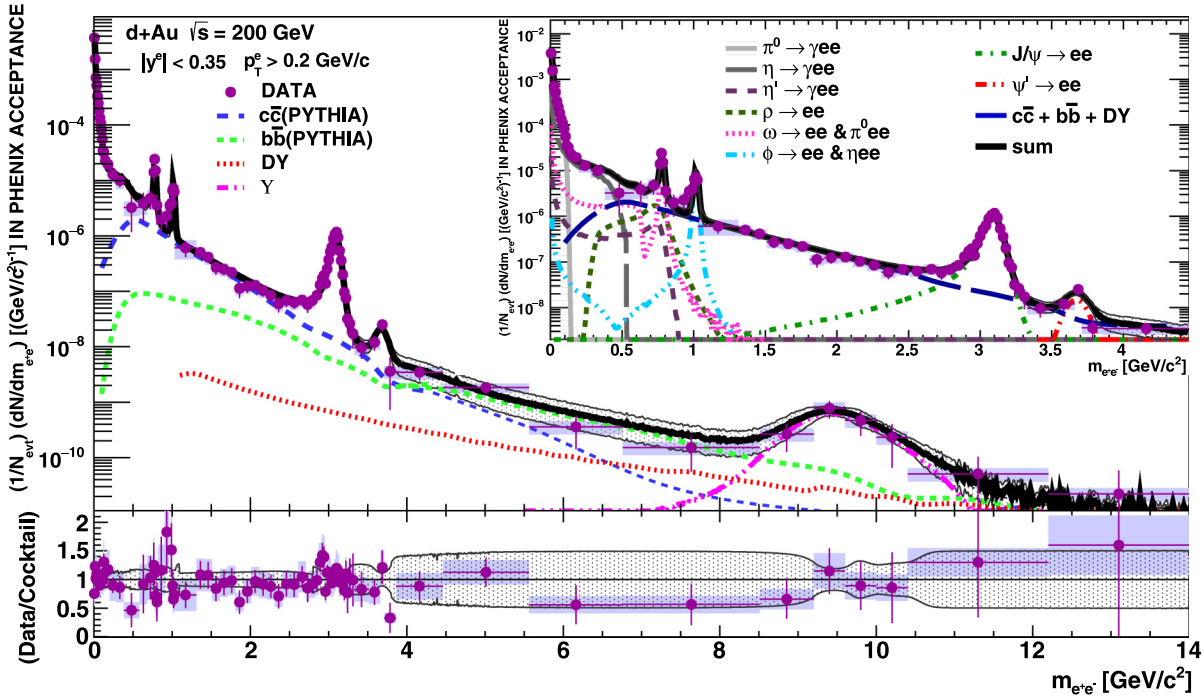

FIG. 4. (Color online) Inclusive e^+e^--pair yield from minimum bias d + Au collisions as a function of mass. The data are compared to our model of expected sources. The inset shows in detail the mass range up to 4.5 GeV/c^2. In the lower panel, the ratio of data to expected sources is shown with systematic uncertainties.

as a benchmark. The cocktail includes pseudoscalar and vector meson decays, semileptonic decays of heavy flavor, and e^+e^- pairs created through the Drell–Yan mechanism.

The pseudoscalar mesons, π^0 and η, and vector mesons, ω, ϕ, J/ψ, and the Υ, are generated based on measured differential $d+\mathrm{Au}$ cross sections [27,35–39]. The contributions from mesons not directly measured in $d+\mathrm{Au}$ (η', ρ, and ψ') are determined relative to the measured mesons (η, ω, J/ψ, respectively) by using particle ratios from $p+p$ or jet fragmentation [22]. Decay kinematics, branching ratios, electromagnetic transition form factors, etc. are based on the most up-to-date information from the Particle Data Group [40]. The yield of e^+e^- pairs created through the Drell–Yan mechanism was simulated by using PYTHIA.[2] For the normalization we use a cross section of 34 ± 28 nb, which was determined by a simultaneous fit of the data at high-mass to Drell–Yan, charm, and bottom contributions by using the PYTHIA simulation. The systematic uncertainty in the Drell–Yan cross section is propagated through the subsequent heavy-flavor cross-section analysis. This uncertainty has a negligible effect (<5%) on the final result of the bottom cross section. As can be seen from Fig. 4, the contribution from Drell–Yan is extremely small below ≈ 5 GeV/c^2. It remains a minor contribution to the dielectron pair spectrum below 10 GeV/c^2.

The double-differential contribution from semileptonic decays of heavy flavor are simulated by using two different $p+p$ event generators, PYTHIA and MC@NLO. The cross sections for $c\bar{c}$ and $b\bar{b}$ in the cocktail shown in Fig. 4 are the ones extracted from this work, as discussed below.

The PYTHIA program generates heavy-quark pairs by calculating the leading order pQCD gluon fusion contributions. We used PYTHIA in forced $c\bar{c}$ or $b\bar{b}$ production mode[3] to match Ref. [22], and CTEQ5L as the input parton-distribution function.

The MC@NLO package (v. 4.03) [33,41] is a next-to-leading-order (NLO) simulation that generates hard scattering events to be passed to HERWIG (vers. 6.520) [42] for fragmentation into the vacuum. Since the package is a two-step procedure consisting of event generation and then fragmentation, care is taken to pass the color flow of each parton configuration from the generator to HERWIG. In addition, since flavor creation (i.e., $qq \to Q\bar{Q}$ and $gg \to Q\bar{Q}$) processes at order α_S^2 can generate some of the higher-order processes through parton showering, MC@NLO keeps track of this to ensure an accurate result. While the default MC@NLO package generates $b\bar{b}$ events, it does not incorporate $c\bar{c}$ events. Thus, we altered

[2]Drell–Yan PYTHIA-6 [32], using parameters MSEL = 0, MSTP(43) = 3, MSTP(33) = 1, MSTP(32) = 1, MSUB(1) = 1, MSTP(52) = 2, MSTP(54) = 2, MSTP(56) = 2, MSTP(51) = 10041 (CTEQ6LL), MSTP(91) = 1, PARP(91) = 1.5, MSTP(33) = 1, MSTP(31) = 1.38, MSTP(32) = 4, CKIN(3) = 0.5, CKIN(1) = 0.5, CKIN(2) = −1.0, CKIN(4) = −1.0, MSTP(71) = 0.

[3]Heavy flavor PYTHIA-6 [32], using parameters MSEL = 4 ($c\bar{c}$) or 5 ($b\bar{b}$), MSTP(91) = 1, PARP(91) = 1.5, MSTP(33) = 1, PARP(31) = 1.0, MSTP(32) = 4, PMAS(4) = 1.25, PMAS(5) = 4.1″

TABLE IV. Number of $c\bar{c}$ pairs at midrapidity in $y_{c\bar{c}} = 1$ and $y_{c\bar{c}} = 0.7$ relative to 4π. $y_{c\bar{c}}$ corresponds to the rapidity of the center of mass of the $c\bar{c}$ pair.

Acceptance	PYTHIA $c\bar{c}$ pairs	MC@NLO $c\bar{c}$ pairs
4π	1	1
$\lvert y_{c\bar{c}}\rvert < 0.5$	0.275	0.297
$\lvert y_{c\bar{c}}\rvert < 0.35$	0.2	0.215

TABLE V. Yields of e^+e^- pairs from $c\bar{c}$ measured in units of one $c\bar{c}$ pair per event divided by the effective semileptonic branching ratio squared $F_{\mathrm{B.R.}}^{c\bar{c}} = [\mathrm{B.R.}(c \to e)]^2$, where B.R. is the effective branching ratio of 9.4%.

Acceptance	PYTHIA e^+e^- pairs from $c\bar{c}$ [$F_{\mathrm{B.R.}}^{c\bar{c}\ -1}$]	MC@NLO e^+e^- pairs from $c\bar{c}$ [$F_{\mathrm{B.R.}}^{c\bar{c}\ -1}$]
4π	1	1
$\lvert y_{e^+}\&y_{e^-}\rvert < 0.5$	0.042	0.035
$\lvert y_{e^+}\&y_{e^-}\rvert < 0.5\&\&$ $m_{e^+e^-} > 1.16$ GeV/c^2	0.0047	0.0022
$\lvert y_{e^+}\&y_{e^-}\rvert < 0.35$	0.021	0.017
$\lvert y_{e^+}\&y_{e^-}\rvert_{\mathrm{PHENIX}}$	0.0023	0.0016
$\lvert y_{e^+}\&y_{e^-}\rvert_{\mathrm{PHENIX}}\&\&$ $m_{e^+e^-} > 1.16$ GeV/c^2	0.00044	0.0002

TABLE VI. Number of $b\bar{b}$ pairs at midrapidity in $y_{b\bar{b}} = 1$ and $y_{b\bar{b}} = 0.7$ relative to 4π. $y_{b\bar{b}}$ corresponds to the rapidity of the center of mass of the $b\bar{b}$ pair.

Acceptance	PYTHIA $b\bar{b}$ pairs	MC@NLO $b\bar{b}$ pairs
4π	1	1
$\lvert y_{b\bar{b}}\rvert < 0.5$	0.39	0.40
$\lvert y_{b\bar{b}}\rvert < 0.35$	0.28	0.29

TABLE VII. Yields of e^+e^- pairs from $b\bar{b}$, measured in units of one $b\bar{b}$ pair per event divided by the effective semileptonic branching ratio squared $F_{\mathrm{B.R.}}^{b\bar{b}} = [\mathrm{B.R.}(b \to e)]^2$, where B.R. is the effective branching ratio of 15.8% using a like-sign pair subtraction, or 22% not considering the like-sign pairs.

Acceptance	PYTHIA e^+e^- pairs from $b\bar{b}$ [$F_{\mathrm{B.R.}}^{b\bar{b}\ -1}$]	MC@NLO e^+e^- pairs from $b\bar{b}$ [$F_{\mathrm{B.R.}}^{b\bar{b}\ -1}$]
4π	1	1
$\lvert y_{e^+}\&y_{e^-}\rvert < 0.5$	0.095	0.091
$\lvert y_{e^+}\&y_{e^-}\rvert < 0.5$ $m_{e^+e^-} > 1.16$ GeV/c^2	0.0425	0.0395
$\lvert y_{e^+}\&y_{e^-}\rvert < 0.35$	0.048	0.046
$\lvert y_{e^+}\&y_{e^-}\rvert_{\mathrm{PHENIX}}$	0.0084	0.0080
$\lvert y_{e^+}\&y_{e^-}\rvert_{\mathrm{PHENIX}}$ $m_{e^+e^-} > 1.16$ GeV/c^2	0.00368	0.0037

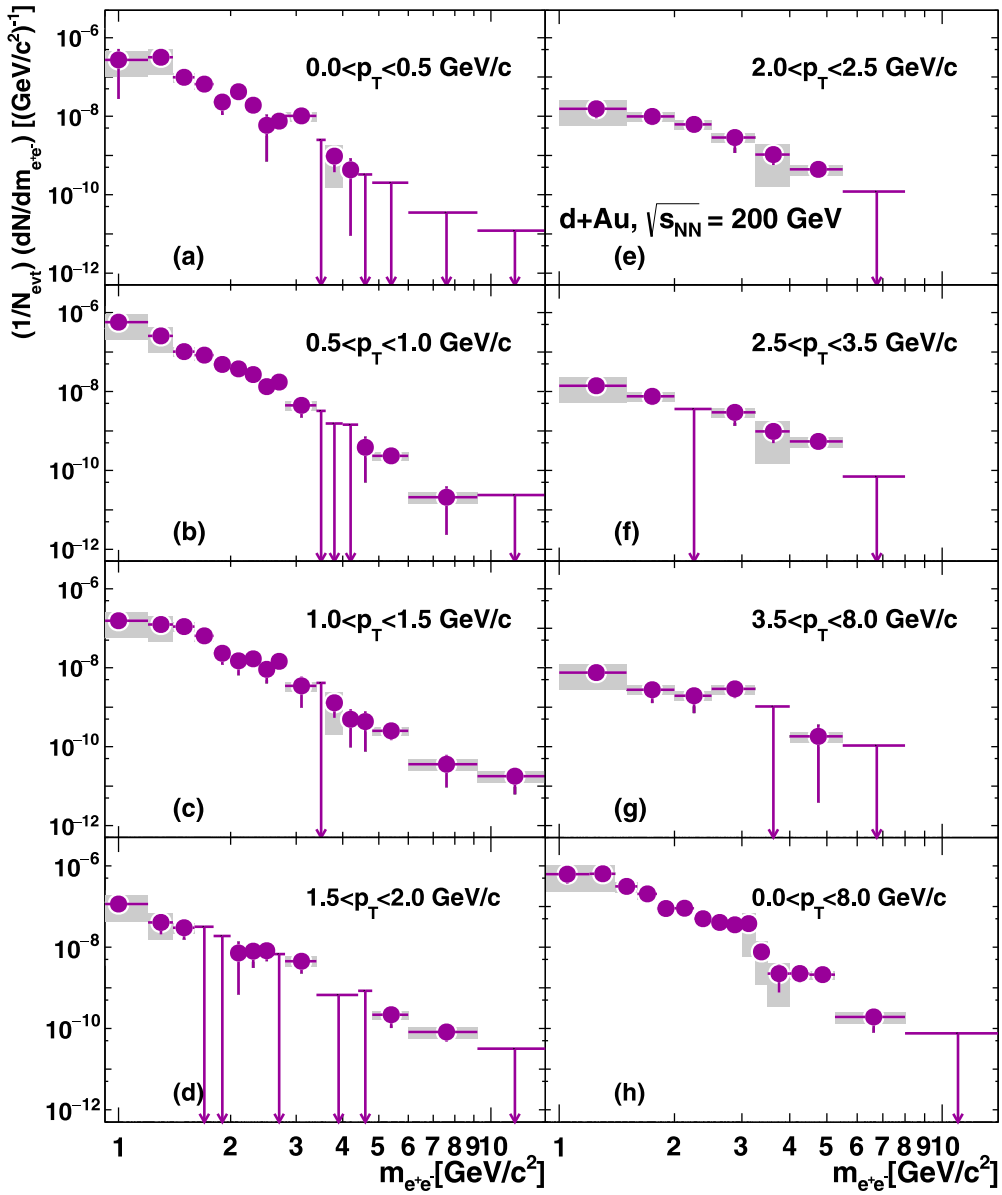

FIG. 5. (Color online) Double-differential e^+e^--pair yield from semileptonic decays of heavy flavor in inelastic d + Au collisions. Shown are mass projections in slices of p_T. The p_T intervals are indicated in each panel. Systematic uncertainties are shown as bars, downward pointing arrows indicate upper limits at 95% confidence limit.

the default package to enable charm production.[4] Because both MC@NLO and HERWIG use the standard PDG process ID codes [40], we changed the process code from -1705 ($H_1H_2 \to b\bar{b} + X$) to -1704 ($H_1H_2 \to c\bar{c} + X$) and adjusted the heavy-quark mass to the charm quark, 1.29 GeV/c^2. No other parameters were modified. In contrast to PYTHIA, the running parameters of MC@NLO do not need to be fine-tuned for different analyses. CTEQ6M [43] was used to provide the input parton-distribution function.

The electrons and positrons from all simulations are filtered through the PHENIX acceptance [28]. The e^+e^--pair acceptance depends on the production process, which determines the correlation between the electron and positron. For pseudoscalar and vector meson decays, the e^+e^- pairs originate from an intermediate virtual photon that correlates the momenta of e^+ and e^-. For e^+e^- pairs from heavy-flavor decays, the correlation is governed by the interplay of two contributions: (i) the QCD production of the $q\bar{q}$ pair, which determines the rapidity distribution of the pair, the rapidity gap between q and $\bar{q}$, and the extent to which they are back to back in azimuthal angle; and (ii) the decay kinematics of the two independent semileptonic decays. The latter tends to randomize the correlation if the mass of the quark is large compared to its momentum. In the limit of very large quark masses the decays will occur at rest and the e^+ and e^- momenta will be determined exclusively by the independent decays. In

[4]This trivial adaptation was reviewed by the original MC@NLO authors via private communication.

contrast, for small quark masses the decay products will be boosted along the momenta of the parent quarks and thus their correlation will closely reflect the correlations between the parent quarks.

The differences between the acceptance for e^+e^- pairs from charm and bottom production are documented in Tables IV to VII. While only 1 out of 500 e^+e^- pairs from charm production is accepted in PHENIX, 1 out of 120 pairs from bottom production is accepted. This can be compared to the limiting case of very large quark masses, for which the direction of the decay e^+ and e^- are independent and approximately 1 of 80 e^+e^- pairs will fall into the PHENIX acceptance. The acceptance for e^+e^- pairs from $b\bar{b}$ is only 30% different from this limiting case, while for $c\bar{c}$ the deviation is more than a factor of five. This suggests that the acceptance for pairs from $b\bar{b}$ is driven mostly by decay kinematics and thus depends only a little on the correlation between the b and $\bar{b}$. Consequently, the model dependence must be much smaller for $b\bar{b}$ than for $c\bar{c}$.

Comparing PYTHIA and MC@NLO in Tables V and VII shows that, indeed, the difference between the acceptance calculated with PYTHIA and MC@NLO is much smaller for $b\bar{b}$ than for $c\bar{c}$ pairs. For bottom production the difference is about 5%, while in the charm case the acceptance is different by a factor of 1.2, which increases to 2.2 if one restricts the mass range to above 1.16 GeV/c^2. Most of this model dependence is already apparent when going from 4π to a restricted rapidity coverage of $\Delta y = 1$ for e^+ and e^- and does not significantly increase when restricting to the smaller PHENIX aperture.

The correlations of the q and $\bar{q}$ are very different in PYTHIA and MC@NLO. While in MC@NLO the correlation is due to including NLO terms explicitly in the pQCD calculation, in the first-order PYTHIA calculation the correlation is largely determined by the specific implementation of intrinsic transverse momentum (k_T). While both models predict similar momentum distributions for the individual q and $\bar{q}$, the opening-angle distributions for the $q\bar{q}$ pairs are different and thus the mass distributions in 4π differ substantially. These differences decrease upon selecting decay e^+e^- pairs that fall in the PHENIX acceptance, so the shape of the mass and p_T distributions from the two models are quite similar. Thus in the PHENIX acceptance, the model differences in the $q\bar{q}$ correlations surface mostly through different fractions of e^+e^- pairs that fall in the acceptance.

For $b\bar{b}$ pairs the decay kinematics have a different effect than for $c\bar{c}$. About 50% of the e^+e^- pairs from $b\bar{b}$ production involve only the decay of the b or $\bar{b}$ quark through the decay chain (3c) from Table II and thus are *a priori* insensitive to the opening angle of the $b\bar{b}$ pair.

Since more than 90% of the B mesons have momenta much smaller than their mass, the decay electron is less likely to move in the same direction as the parent meson. Consequently, the correlation between e^+ and e^- from decays of b *and* $\bar{b}$ through decay chains (1b) and (2b) in Table II is smeared. The fraction of e^+e^- pairs in our acceptance from $b\bar{b}$ is much less sensitive to the correlations between the b and $\bar{b}$. We tested this conclusion by randomizing the correlation between b and $\bar{b}$ and found that the acceptance remains unchanged for $b\bar{b}$ while there is a significant difference for $c\bar{c}$.

Since the acceptance of e^+e^- pairs from $b\bar{b}$ is mostly driven by decay kinematics and not by the model-dependent production mechanism, the fraction of e^+e^- pairs must also be less sensitive to any cold-nuclear-matter effects that alter the b or $\bar{b}$ after they are produced. For the lighter $c\bar{c}$ quarks, the sensitivity to the opening angle between the c and $\bar{c}$ is much larger, implying larger model dependence and consequently cold-nuclear-matter effects may have a larger influence on the distribution of dielectrons from $c\bar{c}$. The results obtained in this analysis seem also insensitive to nuclear modifications of the parton-distribution function; when using EPS09 [44] for the MC@NLO or PYTHIA calculation the acceptance factor for e^+e^- pairs from $b\bar{b}$ and $c\bar{c}$ production change by less than 5%.

The simulated e^+e^- pairs are folded with the experimental momentum resolution as well as with the energy loss due to bremsstrahlung. As a result we obtain the double-differential e^+e^--pair yield for the expected sources that can be directly compared to the measured yield. All components are absolutely normalized, except for the heavy-flavor contributions, which are used to determine the bottom and charm cross

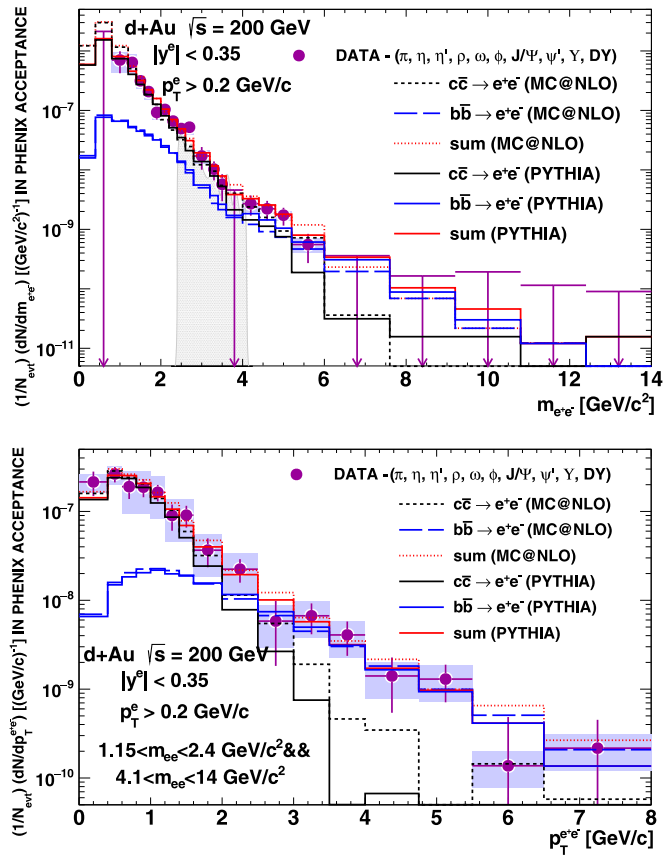

FIG. 6. (Color online) Top panel compares the mass dependence of e^+e^--pair yield with PYTHIA and MC@NLO calculations. The bottom panel shows the comparison for the p_T dependence. The gray panel shown in top panel is not used in the fitting and is excluded in the p_T projection.

section from the e^+e^--pair data, and the Drell–Yan contribution, which is negligibly small and was fixed to be consistent with the data.

C. e^+e^- pairs from heavy-flavor decays

To access the heavy-flavor yield, we subtract the yield of the pseudoscalar and vector mesons as well as the Drell–Yan contribution from the measured dielectron spectra. The subtraction is done double differentially in mass and p_T. The results are shown in Fig. 5 as mass spectra in slices of transverse momentum. The data are plotted above 1.0 GeV/c^2, as lower mass e^+e^- are dominated by hadronic decay contributions. In the mass regions, where the inclusive e^+e^- yield is dominated by vector meson decays, only upper limits can be quoted for the subtracted spectra. We use p_T bins of 500 MeV/c up to $p_T = 3$ GeV/c. Above $p_T = 3.0$ GeV/c, statistical limitations dictate the use of broader p_T bins.

V. HEAVY-FLAVOR CROSS-SECTION DETERMINATION

Figure 6 compares the projections of the e^+e^- yield from heavy-flavor decays onto the mass and p_T axes to the PYTHIA and MC@NLO calculations. The absolute normalization of each calculation was adjusted to the data as discussed below. The shape of the measured distributions is well described by both simulations. Both projections illustrate the fact that bottom production is dominant at high mass or p_T.

In the double-differential spectra, the separation of e^+e^- pairs from charm and bottom decays becomes even more evident. This is illustrated in Fig. 7. At lower pair momenta, charm production dominates the yield below 3 GeV/c^2 mass.

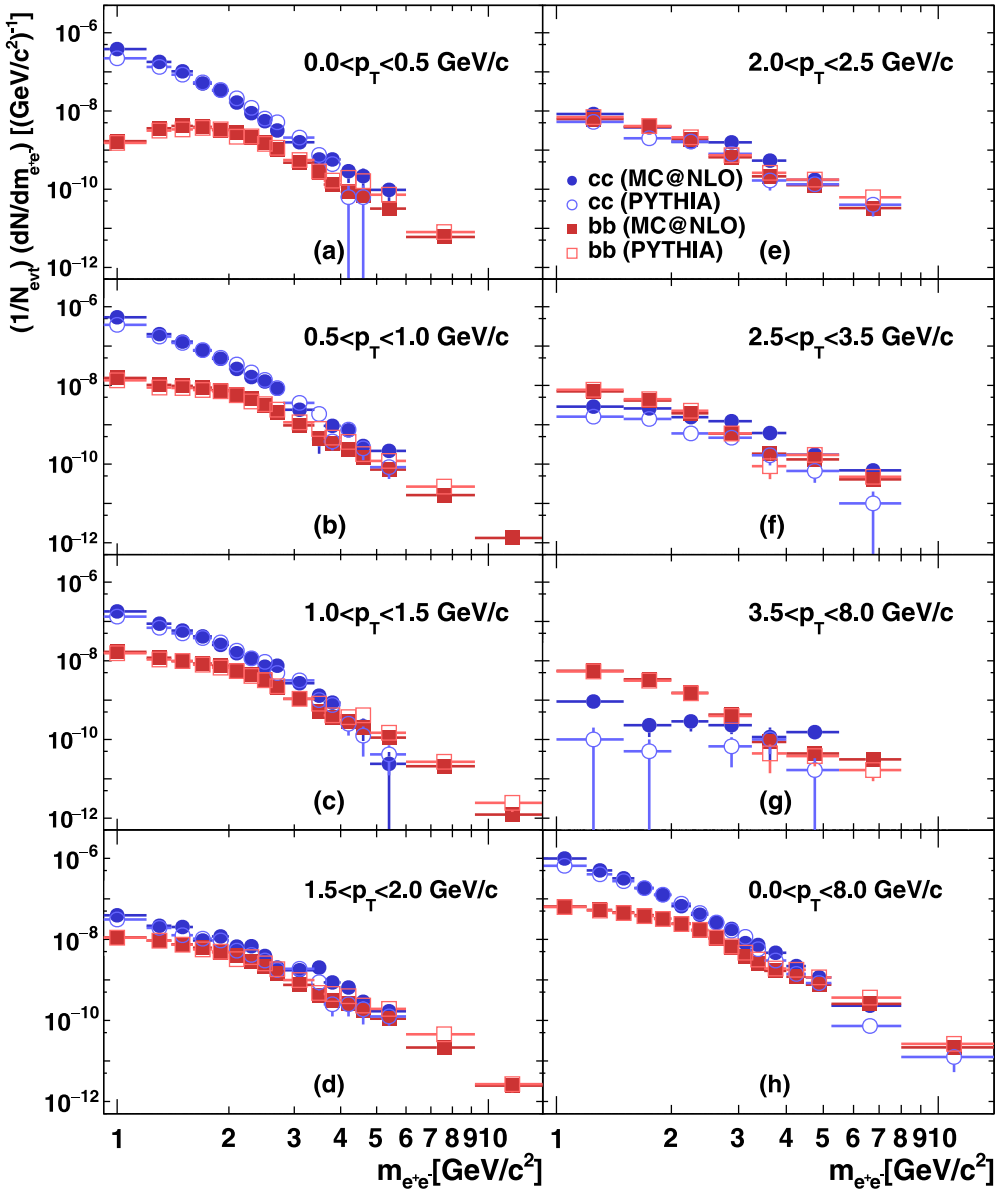

FIG. 7. (Color online) Double-differential e^+e^--pair yield from semileptonic decays of heavy flavor as simulated by PYTHIA and MC@NLO. Shown are mass projections in slices of p_T. The p_T intervals are indicated in each panel.

This dominance vanishes around $p_T = 2$ GeV/c and reverses at higher p_T, where bottom production dominates. Note that this separation of bottom and charm in mass versus p_T is predicted by both generators.

To separate bottom and charm yields quantitatively, we fit the distributions shown in Fig. 7 to the data shown in Fig. 5 with two free parameters, $N_{c\bar{c}}$ and $N_{b\bar{b}}$. These, in turn, are used to determine the charm and bottom cross sections.

The fits are performed according to

$$\left.\frac{dn^{hf}_{e^+e^-}}{dmdp_T}\right|_{\rm PHENIX} = N_{c\bar{c}}\frac{dn^{c\bar{c}}_{e^+e^-}}{dmdp_T} + N_{b\bar{b}}\frac{dn^{b\bar{b}}_{e^+e^-}}{dmdp_T}, \qquad (10)$$

where the left-hand side is the measured yield per minimum-bias triggered event, as shown in Fig. 5. The $n^{c\bar{c}}_{ee}$ and $n^{b\bar{b}}_{ee}$ are determined either by using the PYTHIA simulation or the MC@NLO simulation, where the simulation output was normalized to one $c\bar{c}$ or $b\bar{b}$ pair in 4π. The n_{ee} include the branching ratios for both the quark and antiquark to decay semileptonically. Furthermore, the simulated spectra require that the decay e^+ and e^- each have $p_T > 200$ MeV/c and that both fall into the PHENIX acceptance and satisfy an explicit cut on the pair $m_T > 450$ MeV/c. The fits are performed in the mass range $1.15 < m_{e^+e^-} < 2.4$ GeV/c^2 and $4.1 < m_{e^+e^-} < 14$ GeV/c^2, for both data and simulations. In this normalization scheme, the fit parameters $N_{c\bar{c}}$ and $N_{b\bar{b}}$ are equal to the average number of $c\bar{c}$ pairs and of $b\bar{b}$ pairs per inelastic d + Au event.

The fit results are shown in Figs. 8 and 9 using the PYTHIA and MC@NLO distributions, respectively. Figure 10 shows the ratio of the data points to the MC@NLO simulation. The resulting χ^2 per degree of freedom (NDF) is 147/81

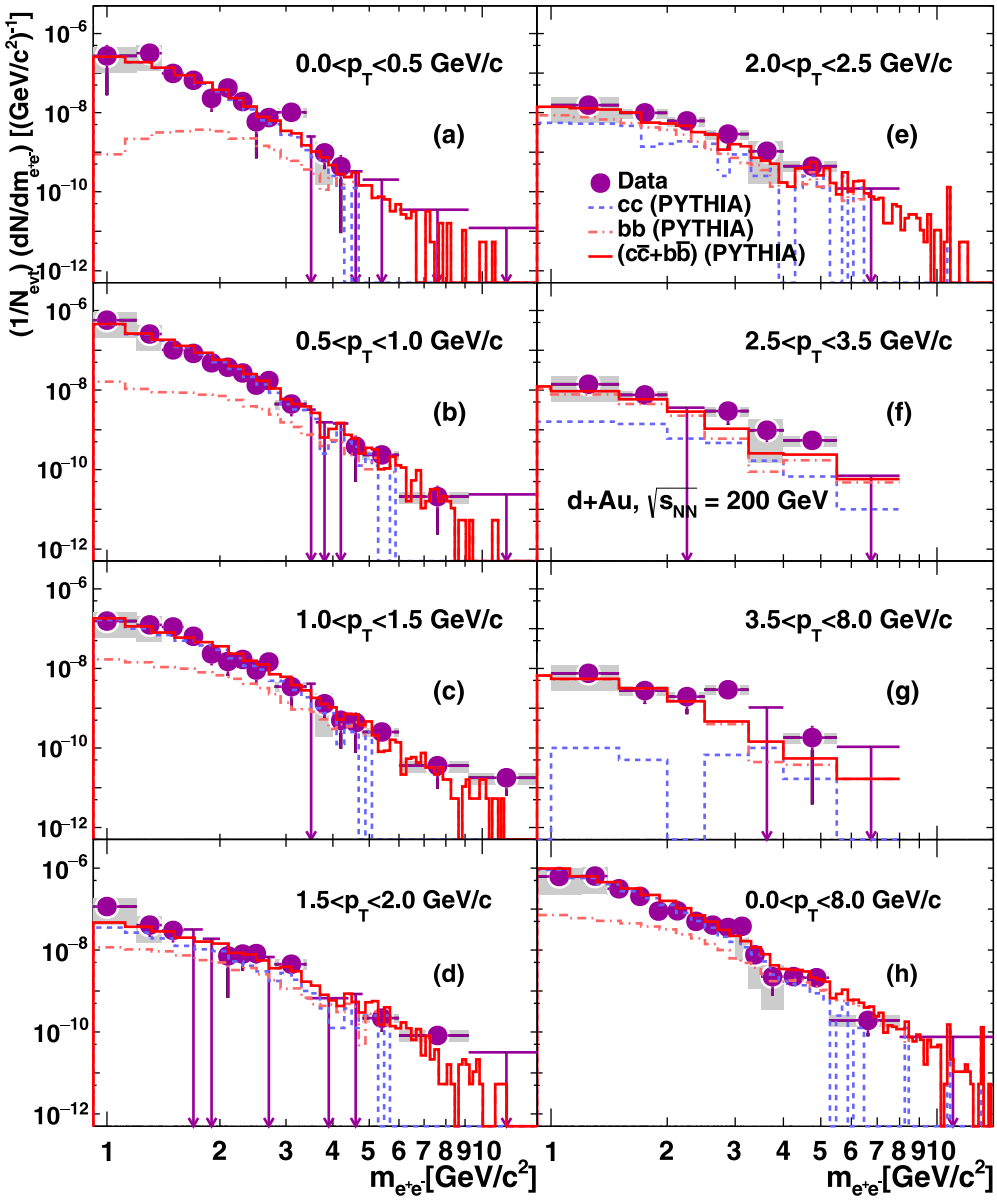

FIG. 8. (Color online) Double-differential e^+e^--pair yield from heavy-flavor decays fit to simulated distributions from PYTHIA. The mass region highlighted by the gray band in Fig. 6 is excluded from the fitting.

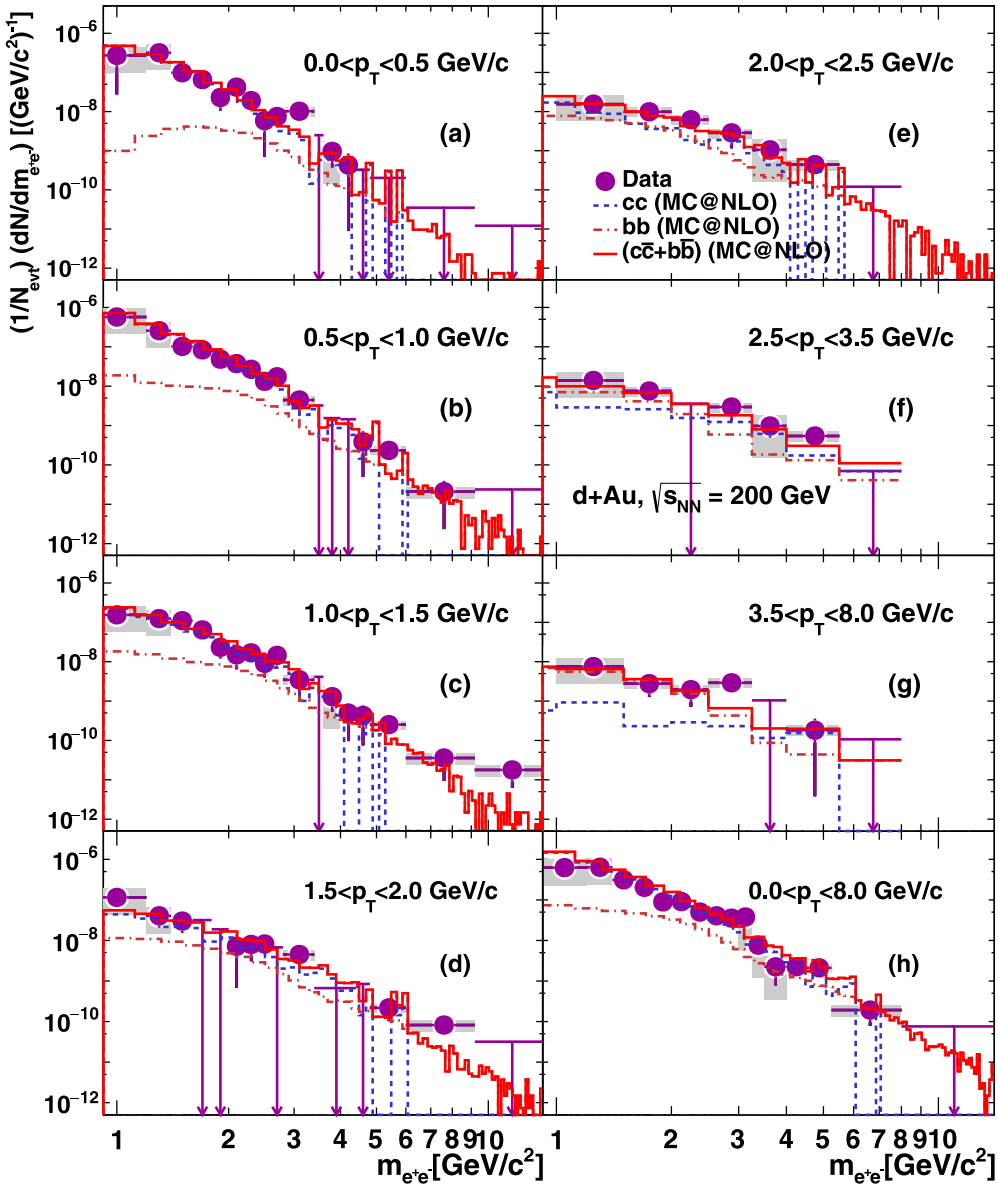

FIG. 9. (Color online) Double-differential e^+e^--pair yield from heavy-flavor decays fit to simulated distributions from MC@NLO. The mass region highlighted by the gray band in Fig. 6 is excluded from the fitting.

for PYTHIA and 162/81 for MC@NLO. This χ^2 is calculated by using statistical uncertainty on the data points only. If we add the systematic uncertainties in quadrature with the systematic uncertainties, the χ^2/NDF is 30/81 and 34/81 for PYTHIA and MC@NLO, respectively. These χ^2/NDF represent extremes because the statistical uncertainty ignores the uncorrelated systematic uncertainty while including the total systematic uncertainty incorrectly includes correlated uncertainties. Because we do not know the fraction of the correlated and uncorrelated systematic uncertainty in the total quoted systematic uncertainty, we conservatively assume that it is entirely correlated and use the fit results from the corresponding case.

For the PYTHIA simulation we obtain the fit parameters

$$N_{c\bar{c}} = 0.069 \pm 0.006(\text{stat}) \pm 0.021(\text{syst}), \quad (11)$$

$$N_{b\bar{b}} = 0.00061 \pm 0.00011(\text{stat}) \pm 0.00019(\text{syst}), \quad (12)$$

and for the MC@NLO

$$N_{c\bar{c}} = 0.172 \pm 0.017(\text{stat}) \pm 0.060(\text{syst}), \quad (13)$$

$$N_{b\bar{b}} = 0.00060 \pm 0.00014(\text{stat}) \pm 0.00020(\text{syst}). \quad (14)$$

The quoted systematic uncertainties were determined by refitting the data points varied up, then down, by one σ_{syst}.

Additional systematic uncertainties arise from the models themselves. In the MC@NLO calculation model uncertainties were evaluated by varying the renormalization scale by a factor of two up and down; the uncertainties are found to be 5% and 2.5% for charm and bottom, respectively. These are quadratically small compared to those arising from the data uncertainties. For PYTHIA no separate evaluation of scale dependence was done.

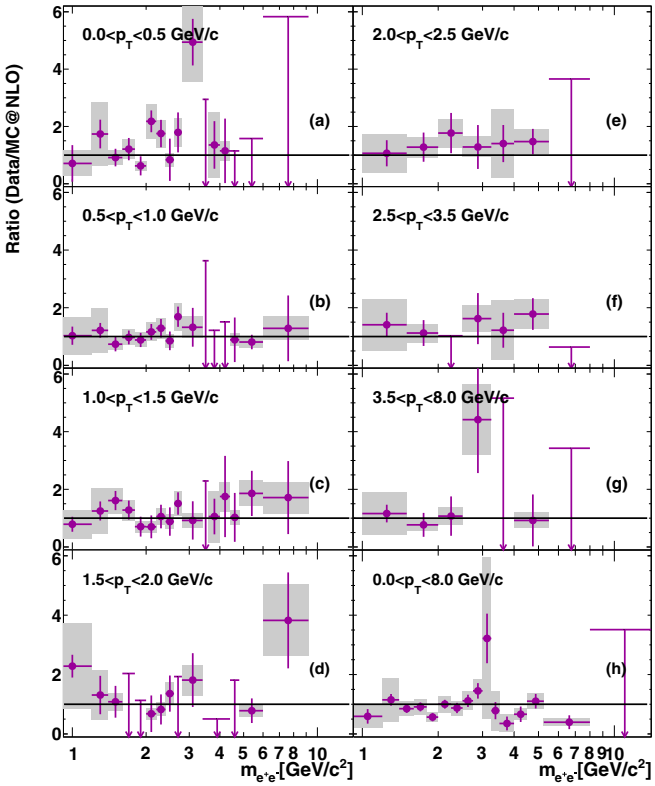

FIG. 10. (Color online) Ratio of the data points (solid magenta points) to the MC@NLO fit (solid red line) shown in Fig. 9.

A second type of model dependence in the cross section arises from the dependence of the pair acceptance on the quark-antiquark correlation from the QCD production process, as discussed above. By comparing results obtained with the different simulations, we can see that the model dependence of the bottom cross sections are less than 2%. For charm production, on the other hand, the extracted cross sections differ by 50%. The large difference in the model dependence of the extracted charm and bottom cross sections results from the fact that the bottom mass is much larger and thus the fraction of e^+e^- pairs that fall into the PHENIX acceptance is dominated by the decay kinematics. For charm production the correlation between c and $\bar{c}$ contribute more significantly.

With the fit parameter $N_{b\bar{b}}$ from above and the acceptance relations in Table VI, we can determine rapidity densities and cross sections for bottom production in d + Au collisions. The cross section follows as

$$\sigma_{b\bar{b}}^{d\mathrm{Au}} = N_{b\bar{b}}\sigma_{\mathrm{inel}}^{d\mathrm{Au}}. \quad (15)$$

We find 1.38 mb and 1.36 mb by using the $N_{b\bar{b}}$ determined by using PYTHIA or MC@NLO, respectively; there is essentially no model dependence in the extracted cross sections. Consequently, we report the bottom-production cross section of

$$\sigma_{b\bar{b}}^{d\mathrm{Au}} = 1.37 \pm 0.28(\mathrm{stat}) \pm 0.46(\mathrm{syst})\mathrm{mb}, \quad (16)$$

TABLE VIII. Comparison of the $p + p$ equivalent $b\bar{b}$ cross section found in this work from d + Au collisions to previously published $b\bar{b}$ cross sections measured in $p + p$ at $\sqrt{s} = 200$ GeV.

$\sigma_{bb}(\mu\mathrm{b})$	Reference
3.4 ± 0.8 (stat)± 1.1 (syst)	This work
$3.2^{+1.2}_{-1.1}$ (stat)$^{+1.4}_{-1.3}$ (syst)	[20]
3.9 ± 2.5 (stat)$^{+3}_{-2}$ (syst)	[22]
4.0 ± 0.5 (stat) $\pm$ 1.1 (syst)	[14]

and a corresponding rapidity density at midrapidity averaged over $\Delta y = 1$ of

$$\left.\frac{d\sigma_{b\bar{b}}^{d\mathrm{Au}}}{dy}\right|_{y=0} = 0.54 \pm 0.11(\mathrm{stat}) \pm 0.18(\mathrm{syst})\mathrm{mb}. \quad (17)$$

The average number of binary collisions is 7.6 ± 0.4 in inelastic d + Au events [25], and the inelastic $p + p$ cross section is $\sigma_{\mathrm{inel}}^{pp} = 42 \pm 3$ mb. The quoted systematic uncertainty on the cross section includes all uncertainties but is dominated by those on the measurement itself.

This is the first measurement of the $b\bar{b}$ cross section in d + Au collisions. One can naively extract a nucleon-nucleon equivalent $b\bar{b}$ cross section and find it to be $\sigma_{bb}^{NN} = 3.4 \pm 0.8\,(\mathrm{stat}) \pm 1.1\,(\mathrm{syst})\,\mu\mathrm{b}$. This value is consistent with the other $b\bar{b}$ cross section values as reported by other measurements, and a comparison is shown in Table VIII.

Cold-nuclear-matter effects have been measured for heavy flavor in d + Au [13,17–19]. In some cases, the effects are small enough to be within the quoted uncertainties of the measurement presented here. In others, they occur at forward or backward rapidity where the effects will not be observed by these data at midrapidity.

The determination of the charm cross section is less reliable due to the large model dependence. By using the PYTHIA calculation we find $\sigma_{c\bar{c}}^{pp} = 385 \pm 34\,(\mathrm{stat}) \pm 119\,(\mathrm{syst})\,\mu\mathrm{b}$ and for the MC@NLO calculation we find $\sigma_{c\bar{c}}^{pp} = 958 \pm 96\,(\mathrm{stat}) \pm 335\,(\mathrm{syst})\,\mu\mathrm{b}$. We conclude that the large model dependence does not allow an accurate determination of the charm cross section from our e^+e^--pair measurement. As shown in Table V, the model dependence of the pair acceptance is already substantial for detection of pairs with mass >1.16 GeV/c^2 in one unit of rapidity. To test predictions for cold-nuclear-matter effects with dilepton data will require comparisons within specific models. Calculations should compare the shape of the predicted e^+e^- mass and p_T spectra to those presented in Figs. 5 and 6.

VI. SUMMARY AND CONCLUSIONS

PHENIX recorded a large sample of e^+e^- pairs from d + Au collisions at $\sqrt{s_{NN}} = 200$ GeV in 2008. The e^+e^--pair yield is consistent with the expected yield from pseudoscalar and vector meson decays and semileptonic decays of heavy mesons. The high statistical precision of the data allows exploration of both the mass and p_T dependence of the e^+e^- yield. Using the double-differential information, we can clearly isolate the contribution of heavy-flavor decays and

determine the fraction of the yield from $c\bar{c}$ and $b\bar{b}$ production. We report the first measurement of the $b\bar{b}$-production cross section in d + Au collisions.

Our procedure utilizes model predictions of the shape of the double differential e^+e^- spectra from $b\bar{b}$ and $c\bar{c}$ production, with a filter requiring that the e^+ and e^- fall inside the PHENIX central arm acceptance. The two simulations used in this work, PYTHIA and MC@NLO, predict very different correlations between the q and $\bar{q}$. In PYTHIA the $q\bar{q}$ correlation is driven by the particular implementation of intrinsic k_T, while in MC@NLO the $q\bar{q}$ correlation arises from including NLO terms in the calculation.

For $b\bar{b}$ production, the fraction of e^+e^- pairs at midrapidity, and therefore also in the PHENIX acceptance, is primarily determined by the decay kinematics of the two independent semileptonic decays and is not sensitive to the substantial model dependence on the $b\bar{b}$ correlations. For the same reason, the fraction of e^+e^- pairs at midrapidity is not sensitive to possible modifications of the momenta for b and $\bar{b}$ due to cold-nuclear-matter effects. Determination of the $b\bar{b}$ cross section thus has little model dependence and the measured e^+e^- double-differential spectra can be used to reliably calculate the production cross section, for which we find

$$\sigma_{b\bar{b}}^{d\mathrm{Au}} = 1.37 \pm 0.28\,(\mathrm{stat}) \pm 0.46\,(\mathrm{syst})\ \mathrm{mb}. \qquad (18)$$

A search for cold-nuclear-matter effects will be possible by comparing the double-differential results reported here with those in $p + p$ collisions. The current result should already help to constrain models of cold-nuclear-matter effects in heavy-quark production.

ACKNOWLEDGMENTS

We thank the staff of the Collider-Accelerator and Physics Departments at Brookhaven National Laboratory and the staff of the other PHENIX participating institutions for their vital contributions. We acknowledge support from the Office of Nuclear Physics in the Office of Science of the Department of Energy, the National Science Foundation, Abilene Christian University Research Council, Research Foundation of SUNY, and Dean of the College of Arts and Sciences, Vanderbilt University (USA), Ministry of Education, Culture, Sports, Science, and Technology and the Japan Society for the Promotion of Science (Japan), Conselho Nacional de Desenvolvimento Científico e Tecnológico and Fundação de Amparo à Pesquisa do Estado de São Paulo (Brazil), Natural Science Foundation of China (P. R. China), Ministry of Education, Youth and Sports (Czech Republic), Centre National de la Recherche Scientifique, Commissariat à l'Énergie Atomique, and Institut National de Physique Nucléaire et de Physique des Particules (France), Bundesministerium für Bildung und Forschung, Deutscher Akademischer Austausch dienst, and Alexander von Humboldt Stiftung (Germany), Hungarian National Science Fund, OTKA (Hungary), Department of Atomic Energy and Department of Science and Technology (India), Israel Science Foundation (Israel), National Research Foundation and WCU program of the Ministry Education Science and Technology (Korea), Physics Department, Lahore University of Management Sciences (Pakistan), Ministry of Education and Science, Russian Academy of Sciences, Federal Agency of Atomic Energy (Russia), VR and Wallenberg Foundation (Sweden), the US Civilian Research and Development Foundation for the Independent States of the Former Soviet Union, the US-Hungarian Fulbright Foundation for Educational Exchange, and the US-Israel Binational Science Foundation.

[1] PHENIX Collaboration, K. Adcox *et al.*, Nucl. Phys. A **757**, 184 (2005).
[2] STAR Collaboration, J. Adams *et al.*, Nucl. Phys. A **757**, 102 (2005).
[3] PHOBOS Collaboration, B. B. Back *et al.*, Nucl. Phys. A **757**, 28 (2005).
[4] BRAHMS Collaboration, I. Arsene *et al.*, Nucl. Phys. A **757**, 1 (2005).
[5] PHENIX Collaboration, K. Adcox *et al.*, Phys. Rev. Lett. **88**, 022301 (2001).
[6] PHENIX Collaboration, S. S. Adler *et al.*, Phys. Rev. Lett. **91**, 072301 (2003).
[7] STAR Collaboration, J. Adams *et al.*, Phys. Rev. Lett. **90**, 172301 (2003).
[8] M. He, R. J. Fries, and R. Rapp, Phys. Rev. C **86**, 014903 (2012).
[9] R. Sharma and I. Vitev, Phys. Rev. C **87**, 044905 (2013).
[10] W. A. Horowitz and M. Gyulassy, J. Phys. G **35**, 104152 (2008).
[11] Y. L. Dokshitzer and D. E. Kharzeev, Phys. Lett. B **519**, 199 (2001).
[12] PHENIX Collaboration, A. Adare *et al.*, Phys. Rev. C **84**, 044905 (2011).
[13] PHENIX Collaboration, A. Adare *et al.*, Phys. Rev. Lett. **109**, 242301 (2012).
[14] STAR Collaboration, H. Agakishiev *et al.*, Phys. Rev. D **83**, 052006 (2011).
[15] ALICE Collaboration, B. Abelev *et al.*, Phys. Rev. D **86**, 112007 (2012).
[16] ALICE Collaboration, D. Thomas, arXiv:1312.1489.
[17] PHENIX Collaboration, A. Adare *et al.*, Phys. Rev. C **89**, 034915 (2014).
[18] PHENIX Collaboration, A. Adare *et al.*, Phys. Rev. C **87**, 034904 (2013).
[19] PHENIX Collaboration, A. Adare *et al.*, Phys. Rev. Lett. **111**, 202301 (2013).
[20] PHENIX Collaboration, A. Adare *et al.*, Phys. Rev. Lett. **103**, 082002 (2009).
[21] STAR Collaboration, M. Aggarwal *et al.*, Phys. Rev. Lett. **105**, 202301 (2010).
[22] PHENIX Collaboration, A. Adare *et al.*, Phys. Lett. B **670**, 313 (2009).
[23] PHENIX Collaboration, K. Adcox *et al.*, Nucl. Instrum. Methods Phys. Res., Sect. A **499**, 469 (2003).
[24] PHENIX Collaboration, K. Adcox *et al.*, Nucl. Instrum. Methods Phys. Res., Sect. A **499**, 489 (2003).
[25] PHENIX Collaboration, A. Adare *et al.*, Phys. Rev. C **90**, 034902 (2014).

[26] PHENIX Collaboration, L. Aphecetche *et al.*, Nucl. Instrum. Methods Phys. Res., Sect. A **499**, 521 (2003).
[27] D. Sharma, Ph.D. thesis, Weizmann Institute of Science, 2010 (unpublished).
[28] PHENIX Collaboration, A. Adare *et al.*, Phys. Rev. C **81**, 034911 (2010).
[29] J. A. Kamin, Ph.D. thesis, Stony Brook University, 2012.
[30] P. Crochet and P. Braun-Munzinger, Nucl. Instrum. Methods Phys. Res., Sect. A **484**, 564 (2002).
[31] D. E. Groom *et al.*, Euro. Phys. J. C **15**, 47 (2000).
[32] T. Sjostrand, S. Mrenna, and P. Z. Skands, J. High Energy Phys. 5 (2006) 026.
[33] S. Frixione and B. Webber, J. High Energy Phys. 6 (2002) 029.
[34] GEANT User's Guide, 3.15, CERN Program Library.
[35] PHENIX Collaboration, S. Adler *et al.*, Phys. Rev. Lett. **98**, 172302 (2007).
[36] PHENIX Collaboration, S. S. Adler *et al.*, Phys. Rev. C **74**, 024904 (2006).
[37] PHENIX Collaboration, A. Adare *et al.*, Phys. Rev. C **84**, 044902 (2011).
[38] PHENIX Collaboration, A. Adare *et al.*, Phys. Rev. Lett. **107**, 142301 (2011).
[39] PHENIX Collaboration, A. Adare *et al.*, Phys. Rev. C **87**, 044909 (2013).
[40] Particle Data Group, J. Beringer *et al.*, Phys. Rev. D **86**, 010001 (2012).
[41] S. Frixione, P. Nason, and B. R. Webber, J. High Energy Phys. 8 (2003) 007.
[42] G. Corcella and B. Webber, J. High Energy Phys. 1 (2001) 010.
[43] M. R. Whalley *et al.*, arXiv:hep-ph/0601012.
[44] K. Eskola, H. Paukkunen, and C. Salgado, J. High Energy Phys. 4 (2009) 065.